PENSOFT.

EVOLUTIONARY SYSTEMATICS

The skull morphology of the Komodo dragon, *Varanus komodoensis* (Reptilia, Squamata, Varanidae) — a digital-dissection study

Momoko Kubota[1], Jakob Hallermann[2], André Beerlink[3], Alexander Haas[1,2]

1   *Universität Hamburg, Edmund-Siemers-Allee 1, 20146 Hamburg, Germany*

2   *Leibniz-Institute for the Analysis of Biodiversity Change (LIB), Zoologisches Museum Hamburg, Martin-Luther-King-Platz 3, 20146 Hamburg, Germany*

3   *Comet Yxlon GmbH, Essener Bogen 15, 22419 Hamburg, Germany*

https://zoobank.org/0D9D21E5-7DE5-4EEF-AFE0-B0A06FC032EC

Corresponding author: Momoko Kubota (momoko.kubota525@gmail.com)

Abstract

This study reports the cranial skeletal morphology of *Varanus komodoensis* Ouwens, 1912. Employing a high-resolution CT scan with subsequent use of 3D data visualization and analysis software, we generated a comprehensive 3D representation of the skull. Reconstruction of the osteoderm and 30 paired and unpaired bones was undertaken, and a detailed examination, comparison, and discussion of these structures were conducted in the context of existing literature. Special attention was given to morphological adaptations and phylogenetic relationships.

The cranial morphology of *V. komodoensis* exhibits a pronounced adaptation to feeding behavior, characterized by a highly fenestrated skull and sharp ziphodont teeth, presumably optimized for the species' distinctive hold-and-pull feeding technique.

Several anatomical indicators of cranial kinesis were identified in the skull of *V. komodoensis*. The absence of the lower temporal bar is linked to the evolution of streptostyly, enabling the free oscillation of the quadrate. The lack of an osteoderm at the frontoparietal suture and the disruption of the postorbital bar provide evidence of mesokinesis. Additionally, loose connections in various cranial segments and the long mandible were interpreted as mobile connections, possibly facilitating the adaptation for swallowing large prey objects.

A review of character states from existing literature reveals synapomorphies between the skull of *Varanus komodoensis* and the extinct *V. priscus* (*Megalania*) Owen, 1859, and also complemented the autapomorphic character states characteristic of the genus *Varanus*.

Key Words

Introduction

Skeletons contain extensive information capable of elucidating diverse biological inquiries. Comparative skeletal studies can demonstrate the general sequence and events in vertebrate phylogeny, and may highlight evolutionary trends characterizing successive major taxa. Overlapping advantageous variations continuously refine the gradually evolving general pattern. Over time, skeletal characters frequently mirror specific adaptations stemming from the species' interaction with their environment and lifestyle (Hildebrand and Goslow 2004).

The skull, a pivotal component of the skeleton, serves several crucial functions. Its composition and shape yield a wealth of biological insights, particularly regarding the organism's adaptation to feeding behavior. Viewing the skull as an apparatus for food intake brings attention to its cranial kinesis, a subject captivating researchers for a century (De Jong and Brongersma 1927; Mertens 1942b; Metzger 2002; Iordansky 2011). In terms of cranial kinesis research, the Lepidosauria stands out as one of the

most extensively studied vertebrate groups, and monitor lizards, in particular, have often been used as example taxa for describing cranial kinesis in Lepidosauria (Smith 1980; Metzger 2002).

Cranial kinesis involves movements of joints or composite units within the skull. The mobility of cranial elements, excluding the temporomandibular joint and ossicles, engages dermatocranium elements in diverse ways. Three primary classifications—prokinesis, mesokinesis, and metakinesis—are distinguished by the location of intracranial joints. In prokinesis the intracranial joint is located in front of the orbit, while mesokinesis features an intracranial joint between the frontal and parietal (behind the orbit). Metakinesis involves joints between the dermatocranium and neurocranium, with the intracranial joint positioned at the rear of the skull. Generally linked to food intake, cranial kinesis closely associates with features of dentition and musculature. In reptiles consuming plant parts or dealing with hard food, like turtles and crocodiles, respectively, cranial kinesis is often underdeveloped or lost (Starck 1979).

The skull morphology of monitor lizards, as well as geckos, has been characterized as highly mesokinetic (Starck 1979). In contrast, the skull of *Varanus komodoensis* has been classified as amphikinetic, exhibiting both mesokinesis and metakinesis (Mertens 1942a). Monitor lizard skulls are further distinguished by streptostyly, where the quadrate is movably connected to the cranium (Frazzetta 1963; Starck 1979). This mobile quadrate allows for significantly increased cranial kinesis in concert with the remarkable intramandibular joints and its movements. The dentary of monitor lizards exhibits loose articulations (streptognathy) with other dermal mandibular bones. This structural arrangement enables intramandibular movements, facilitating the expansion of the mouth floor through the outward rotation of the posterior lower jaws (Starck 1979). The mobility in the mandible allows monitor lizards to ingest large food items beyond the capacity of other lizards (Pianka et al. 2004).

Varanus komodoensis, commonly known as the Komodo dragon, is the best-known and largest representative among monitor lizards. Despite its conspicuous size, it eluded scientific attention until 1910 when a Dutch officer stationed on Flores (Indonesia) reported the existence of exceptionally large monitor lizards on the neighboring island of Komodo (Bennett 1996). Formally described as *V. komodoensis* by Pieter Ouwens in 1912, the director of the zoological collection at Bogor, East Java, the report was based on photographs and a skin description of an adult specimen from Komodo Island (Pianka et al. 2004). Since then, *V. komodoensis* has attracted the attention of numerous researchers. The first cranial description of adult *V. komodoensis* was provided by de Jong and Brongersma (1927) and Lönnberg (1928). In 1942, the German herpetologist Robert Mertens meticulously documented the cranial morphology of *V. komodoensis* in a trilogy of books focusing on various monitor lizards. Later, American biologist Walter Auffenberg contributed

valuable information on the species in his important book (Auffenberg 1981).

With a body length reaching up to three meters and males weighing over 70 kg, *V. komodoensis* inhabits the small Indonesian islands of Komodo, Rintja, Gillimontang, Padar, and the western tip of Flores Island. The fossil record suggests its presence on Flores since the mid-Pleistocene, possibly having inhabited Timor and Java as well (Pianka et al. 2004). The species predominantly preys on large mammals such as goats, deer, pigs, horses, and water buffalo. Today the Komodo dragon stands as one of the most endangered lizard species. Rapid habitat loss and emerging climate change threaten its populations on Indonesian islands (Purwandana et al. 2014). In the 1970s, the total population of Komodo dragons was estimated to be less than 6000 individuals (Auffenberg 1981). According to the International Union for Conservation of Nature (IUCN), in 2021, the population comprised approximately 1400 sexually mature and 2000 juvenile individuals. The Red List of Threatened Species classified the Komodo dragon as critically endangered in 2019, primarily due to habitat reduction.

Previous morphological studies on *Varanus komodoensis* have significantly contributed to our understanding of its anatomy. However, some studies were hindered by the recurrent loss and damage of bone segments (Mertens 1942b). Achieving reliable morphological insights necessitates the visualization and quantification of intact and complete specimens. In this context, 3D digital reconstruction is a crucial tool, providing non-invasive information in contrast to traditional dissection methods, both for hard and soft tissues. Recent advances in imaging techniques, particularly in the field of X-ray microcomputed tomography (CT), have substantially deepened our comprehension of organism morphology within both biological and paleontological contexts (among many others, e.g., Klinkhammer et al. 2017; Broeckhoven and du Plessis 2018).

Surprisingly, the history of CT scans in herpetology is relatively recent, with regular applications commencing only around 2005 and subsequently experiencing exponential growth (Broeckhoven and du Plessis 2018). The use of an industrial CT scanner in 1995 marked the first instance of studying the cranial anatomy of the Mississippi alligator (*Alligator mississippiensis* Daudin, 1801), as published by Rowe et al. (1999) and Brochu (1999). The first micro-CT scan in herpetology was conducted on Arizona night lizards (*Xantusia arizonae* Klauber, 1931) and geckos of the genus *Sphaerodactylus* preserved in amber in 1997 and 1998, respectively, yet the latter findings were not published until two years later (Grimaldi et al. 2000; in Broeckhoven and du Plessis 2018).

In this study, we applied CT and 3D visualization techniques to examine the skull morphology of an individual *Varanus komodoensis* from the Zoological Museum Hamburg's collections. Our objectives were threefold: (1) to provide a detailed description and visualization of cranial bones in *V. komodoensis*; (2) to identify morphological features associated with the species' specific lifestyle,

particularly its unique feeding behavior; and (3) to evaluate the cranial features of *V. komodoensis* in the context of its phylogenetic position, discussing potential apomorphic character states. To achieve these goals, we generated a highresolution CT dataset of the specimen's skull, enabling the demonstration of interconnections among bone elements and the electronic dissection of individual bones from the anatomical context for a comprehensive understanding of their shape characteristics.

Materials and methods

The *Varanus komodoensis* specimen utilized in this investigation originated from the progeny of a captive breeding program at the Washington Zoo and was subsequently relocated to the Berlin Zoological Garden in October 1995. The specimen, a female, had a body mass of 2.56 kg and a total length of 750 mm at the time of transfer. The monitor lizard succumbed at the Berlin Zoological Garden on July 4th, 2001. Following its demise, the specimen was generously donated and transported to the Zoological Museum Hamburg (ZMH). From 2001 to 2023, it has been preserved in a frozen state at the ZMH. The total body length at the commencement of our investigation measured 2030 mm. However, the extended period of frozen storage induced a freeze-drying effect, resulting in specimen stiffening and potential shrinkage. The animal is cataloged within the herpetological collection of the Zoological Museum Hamburg under the catalogue number ZMH R13322.

CT scanning

CT scans and subsequent 3D reconstructions serve as invaluable tools for non-destructive morphological examination. These contemporary techniques facilitate the creation and dissection of a 3D model without causing harm to the specimens. Unlike traditional dissection methods, digital reconstruction obviates the need for specific technical skills but necessitates proficiency in software usage. Appropriately prepared datasets enable seamless access for morphological examination, and their online sharing is independent of temporal or geographical constraints. Despite the method's substantial advantages for morphological analysis, the effective use of files is impeded by substantial file sizes. To generate an anatomically detailed 3D model, high-resolution CT scans are imperative.

The CT scan of the specimen was conducted at Comet Yxlon GmbH in Hamburg, Germany, utilizing a high-resolution Comet Yxlon FF85 CT scanner equipped with a Comet Yxlon 450 kV mini-focus X-ray tube and a Varex Imaging 4343HE detector. A total of 3420 crosssectional images, each sized at 9.4 MB, were computed from the CT scan, forming the basis for the subsequent volume reconstruction. Among these, 2768 images of the skull were employed for segmentation, resulting in an initial dataset size of 26.02 GB.

The cone beam CT scan settings included a stop and go scan type, an X-ray tube power set at 570.0 W (operating at 300 kV source voltage and 1900 µA current for the X-ray beam), with no filter. Projections sized at 3052 px x 3052 px, an exposure time of 400 ms (detector frame rate of 2.5 Hz) for each, and the total scan duration was 01:59:27 h. With a magnification factor of 1.5 and a physical detector pixel size of 0.139 mm x 0.139 mm, the setup yielded data with a general voxel size of 0.0926 mm x 0.0926 mm x 0.0926 mm. All measurements were calculated from voxel size.

Segmentation and visualization

AMIRA 6.2.0 (Thermo Fisher Scientific 2016), a 3D data visualization, and analysis software, was used for the segmentation of the CT volumetric dataset and the creation of a comprehensive 3D volume model of the skull and its individual bones. Each bone underwent independent segmentation. The segmentation process was executed on a workstation featuring a 2.60 GHz CPU (two processors), 128 GB RAM, and operated on the Windows 7 Professional operating system.

For segmentation, the AMIRA tool "Magic Wand" was employed. The Magic Wand tool, functioning as a region-growing algorithm, initiates from a designated starting point, selecting contiguous voxels within a specified gray value tolerance interval. This tool is particularly effective for isolating a singular material within the image. Nevertheless, when bones closely neighbored each other with similar gray values, the algorithm faced challenges in proper separation. In such instances, the "Draw limit line" function was employed, allowing manual drawing of lines in the image for visual separation of closely adjacent, but clearly separate elements. We carefully double-checked that all bone materials were assigned to the proper bone element.

This process was iteratively applied at each level throughout the dataset until distinct skull bone segments were achieved. Following segmentation, the polymesh 3D representation of the segmented objects was reconstructed. The "Generate Surface" function automatically extracted polygon surfaces from the segmentation results. However, to address issues of excessive triangle numbers in the constructed polygon surface, the "Simplification Editor" function was utilized to reduce triangle count. The slightly simplified surface was then rendered visually using the "Surface View" function.

Despite the substantial RAM available, the handling of data during segmentation with AMIRA 3D software occasionally encountered challenges, resulting in software crashes. Despite the relatively high image resolution of the CT scans, the fine serrations of the teeth remained challenging to render in the 3D model. While increasing image resolution could potentially address these issues, it would exponentially inflate file sizes, rendering them unwieldy and difficult to manage.

Results

The skull of *Varanus komodoensis* approximates a blunt pyramidal shape, with the contour in all four aspects (dorsal, ventral, lateral) approximately triangular, tapering anteriorly (Figs 1, 2). The tip of the nose is rounded. Overall, the skull is strongly built, but it has several large windows, especially in the narial region and the posterior part of the skull. The skull of specimen ZMH R13322 measures 16.72 cm in length, 8.3 cm in width, and 6.46 cm in height (orthogonal projection views in Fig. 1). Note in the description below, that cartilage, soft tissue and ligaments were not detected in the CT data. Therefore, small gaps between certain bones could be filled with such tissues.
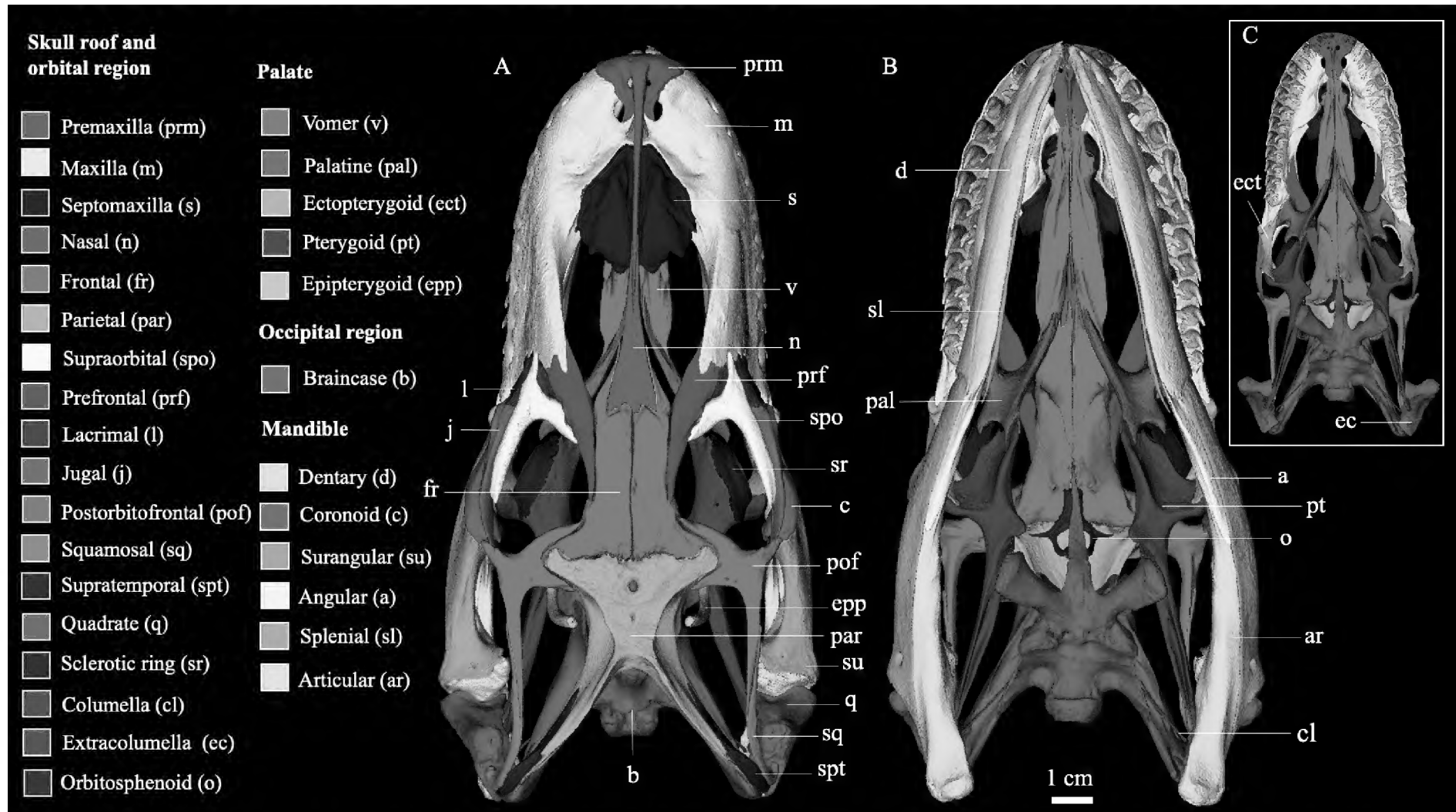
Figure 1. Skull of *Varanus komodoensis* (ZMH R13322). **A.** In dorsal; **B.** In ventral views; **C.** Ventral view without jaw elements. 3d visualization of surface polygon meshes of individually segmented bone elements derived from the CT dataset in orthogonal projections. Scale bar: 1 cm.
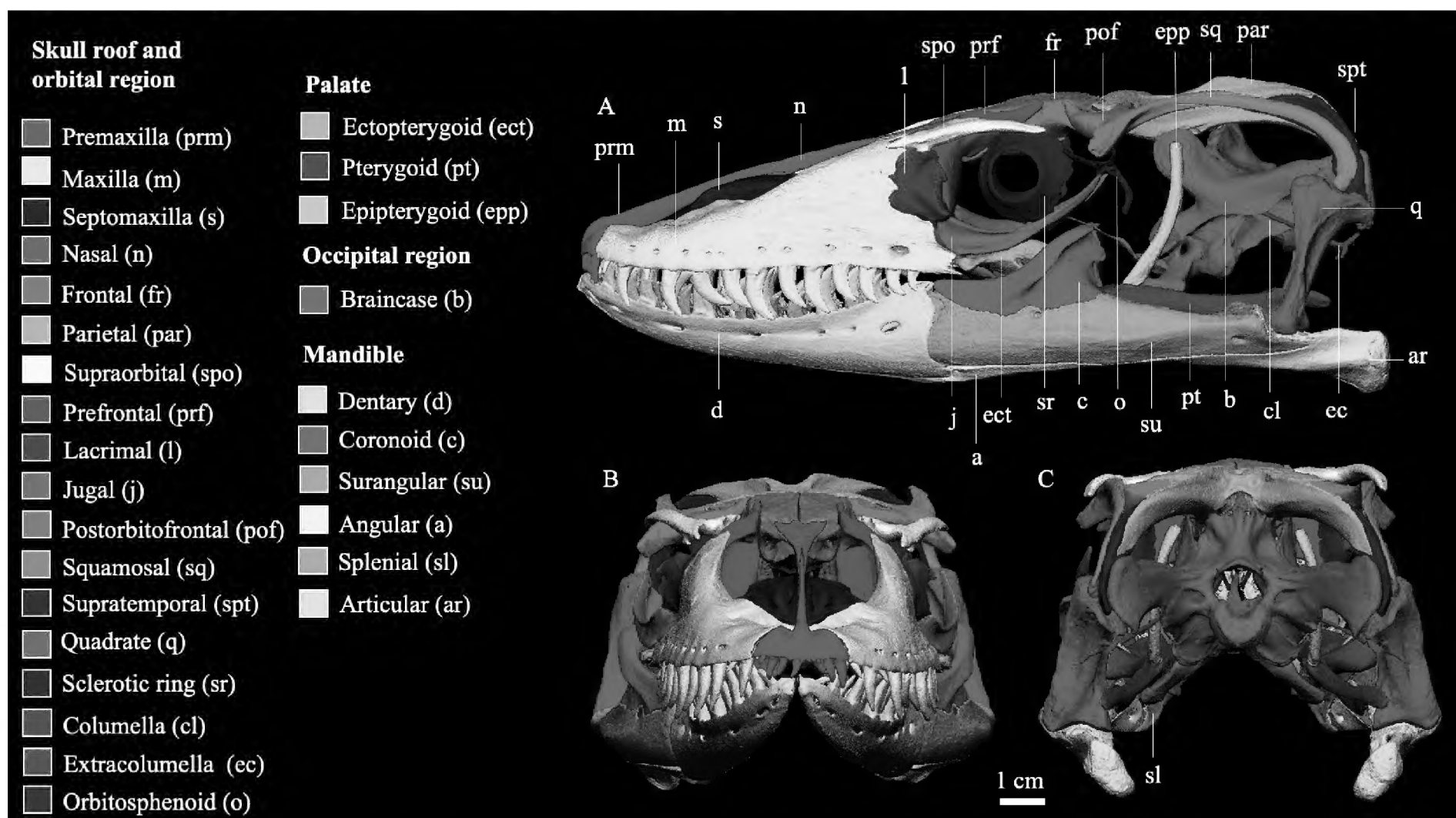
Figure 2. Skull of *Varanus komodoensis* (ZMH R13322). **A.** In lateral; **B.** In anterior; **C.** In posterior views. Orthogonal projections. Scale bar: 1 cm.

Osteoderm

The skull of *Varanus komodoensis* is almost completely covered by osteoderm (Fig. 3) (Maisano et al. (2019)). The shape of the individual osteoderm elements varies greatly with the region of the head. While on the dorsal side of the rostrum bony elements have a much larger, flattened, rosette-like structure (Fig. 3A), on the posterior part of the nasal, they have a simpler, plate-like structure (Fig. 3A).

In the occipital region, various structures occur: rosette-shaped, plate-shaped, and dendritic (Fig. 3A). Laterally, the osteoderm is composed of long, narrow, vermiform structures arranged obliquely in the horizontal direction (Fig. 3C). Ventrally, vermiform elements are also present, with these elements being smaller and more densely arranged compared to the other parts (Fig. 3D). The osteoderm is reduced or absent in the parietal area, frontoparietal suture, parietal foramen, some anterior and lateral areas of the snout, labial margins, and ears. It does not make contact with the underlying cranial bones.

Skull roof and orbital region

The premaxillae are indistinguishably fused into one medial bone element. It is located medially between the most anterior margin of the maxillae and consists of two parts (Fig. 4). The anterior component features a maxillary process extending laterally (Fig. 4A), which tapers posteriorly and forms a suture with the maxilla. The posterior end of the anterior part bears flattened vomero-maxillary processes (Fig. 4B), confluent at their anterior base but bifurcating posteriorly. The vomero-maxillary process is adjacent to both the vomer and the maxilla. Medially, this process has a prominent paired dorsal premaxillary foramen (Fig. 4A), with an additional smaller foramen anterior to it. The ventral face forms an incisive process (Fig. 4B). The anterior margin of the fused premaxillae bears a total of eight teeth, four per side. Additionally, replacement teeth of smaller size are positioned immediately posterior to the functional teeth. The posterior part of the premaxilla consists of the long nasal process (Fig. 4A). This process resembles a dagger in shape, narrow, laterally compressed, and articulates with the septomaxilla ventrally and the nasal laterally, terminating in a sharp point at its posterior end.

The maxilla, a large paired toothed bone, constitutes nearly half the length of the skull (Fig. 5). Anteriorly, the premaxilla, vomer, and septomaxilla are in sutural contact with the maxilla, while posteriorly, the prefrontal, lacrimal, jugal, palatine, and ectopterygoid articulate with it.

The ventral margin of the maxilla features ten horizontally aligned supralabial foramina (Fig. 5B), with the most posterior one exhibiting a significantly larger diameter than the anterior ones.
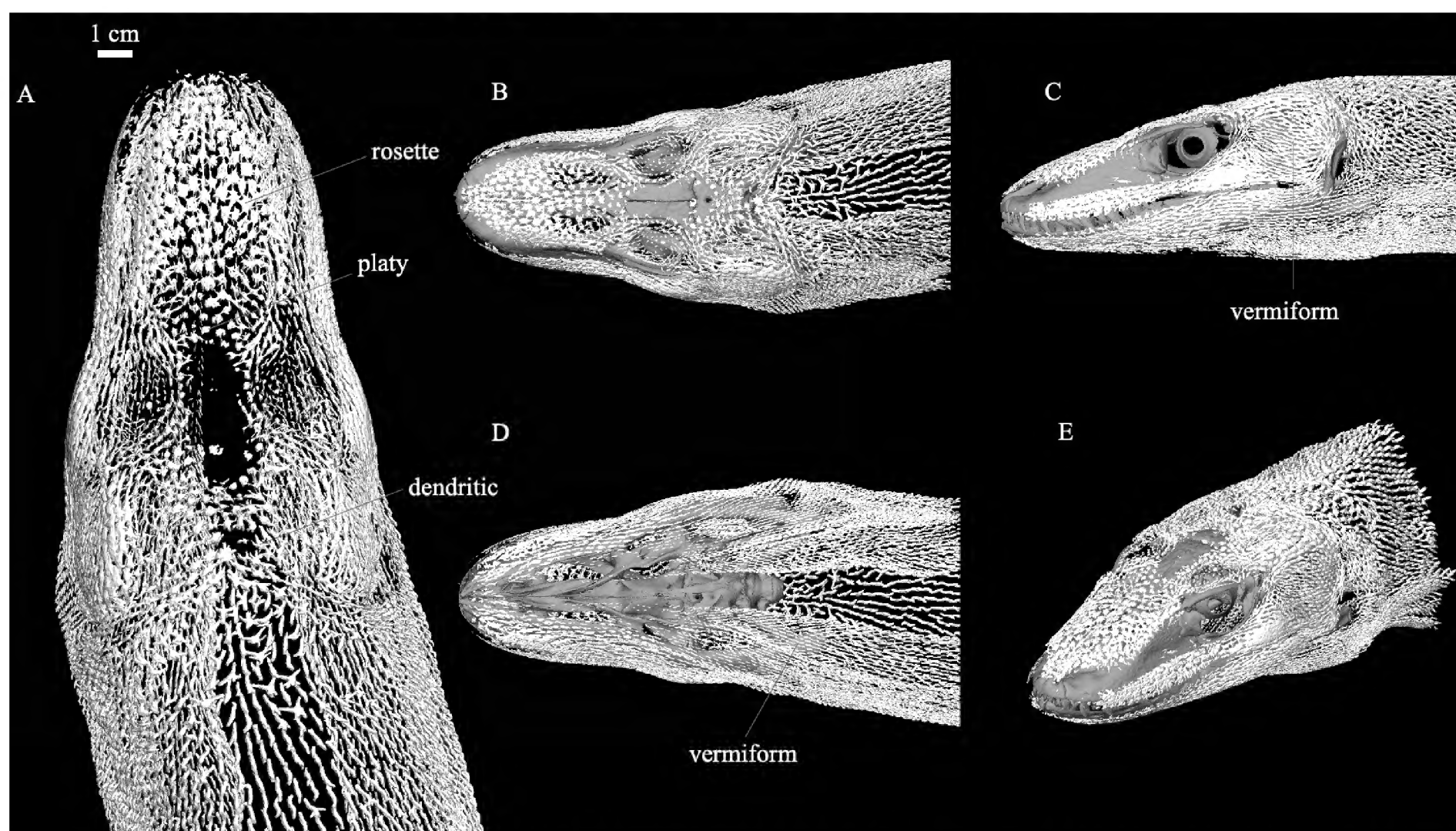
Figure 3. The osteoderm in *Varanus komodoensis* (ZMH R13322) exhibits a finely structured osteoderm armor, characterized by diverse shapes of individual osteoderm elements. **A.** Osteoderm in dorsal view; **B.** Osteoderm and skull in dorsal; **C.** In lateral; **D.** In ventral; **E.** In anterodorsal views. We point out that the lateral portion of the osteoderm, extending from the orbit to the nasal opening, remains unreconstructed in our project. This omission is attributed to the intricate structure of the platelets in this region, the difficulties to reconstruct them accurately, and the constraints imposed by the limited project timeframe. For comparison, we refer readers to Maisano et al. (2019). Scale bar: 1 cm (**A**).
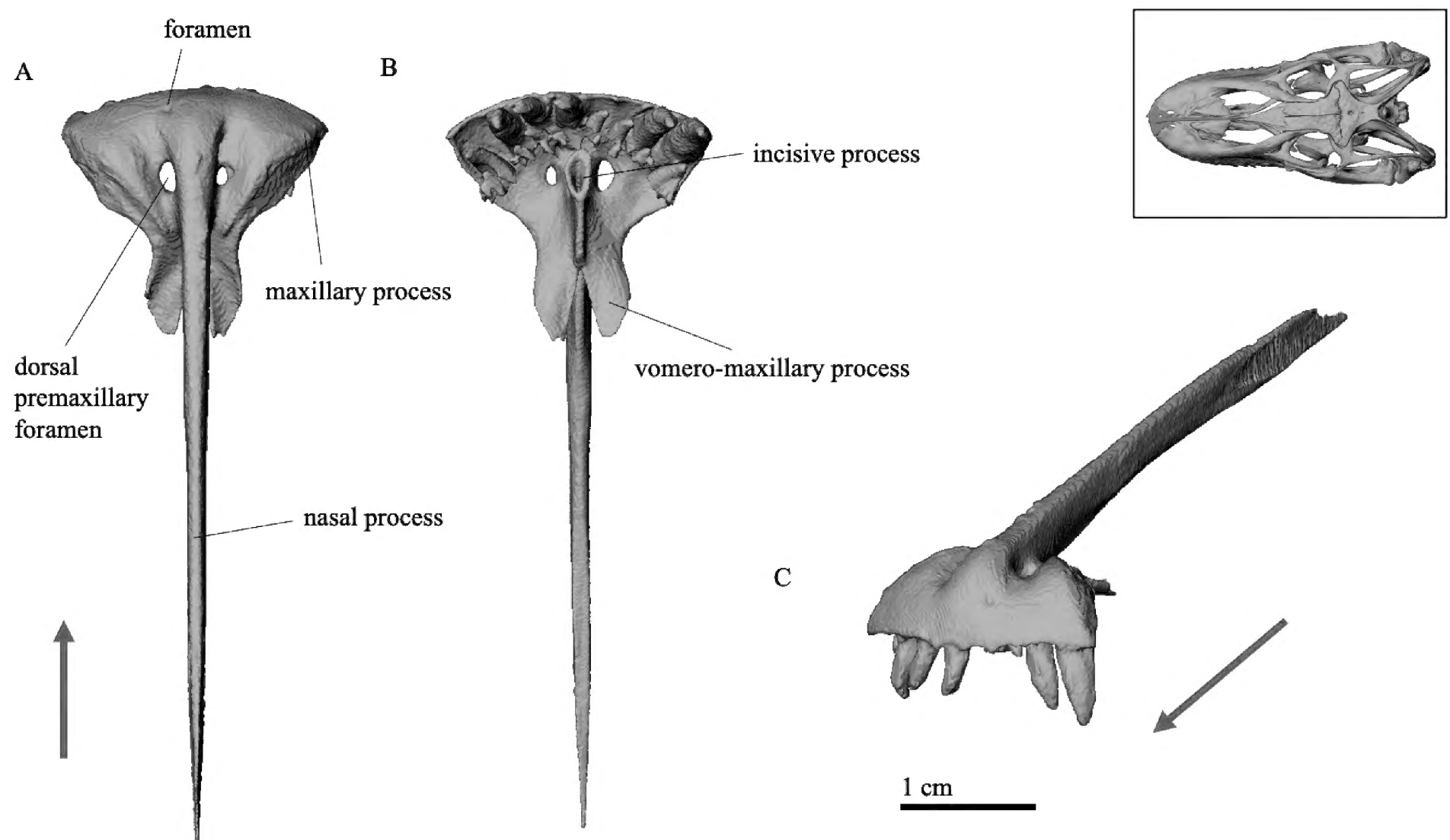
Figure 4. Premaxilla, 3d reconstruction from CT dataset. **A.** In dorsal; **B.** In ventral; **C.** In anterodorsal views. Arrow indicates the anterior direction. Scale bar: 1 cm.
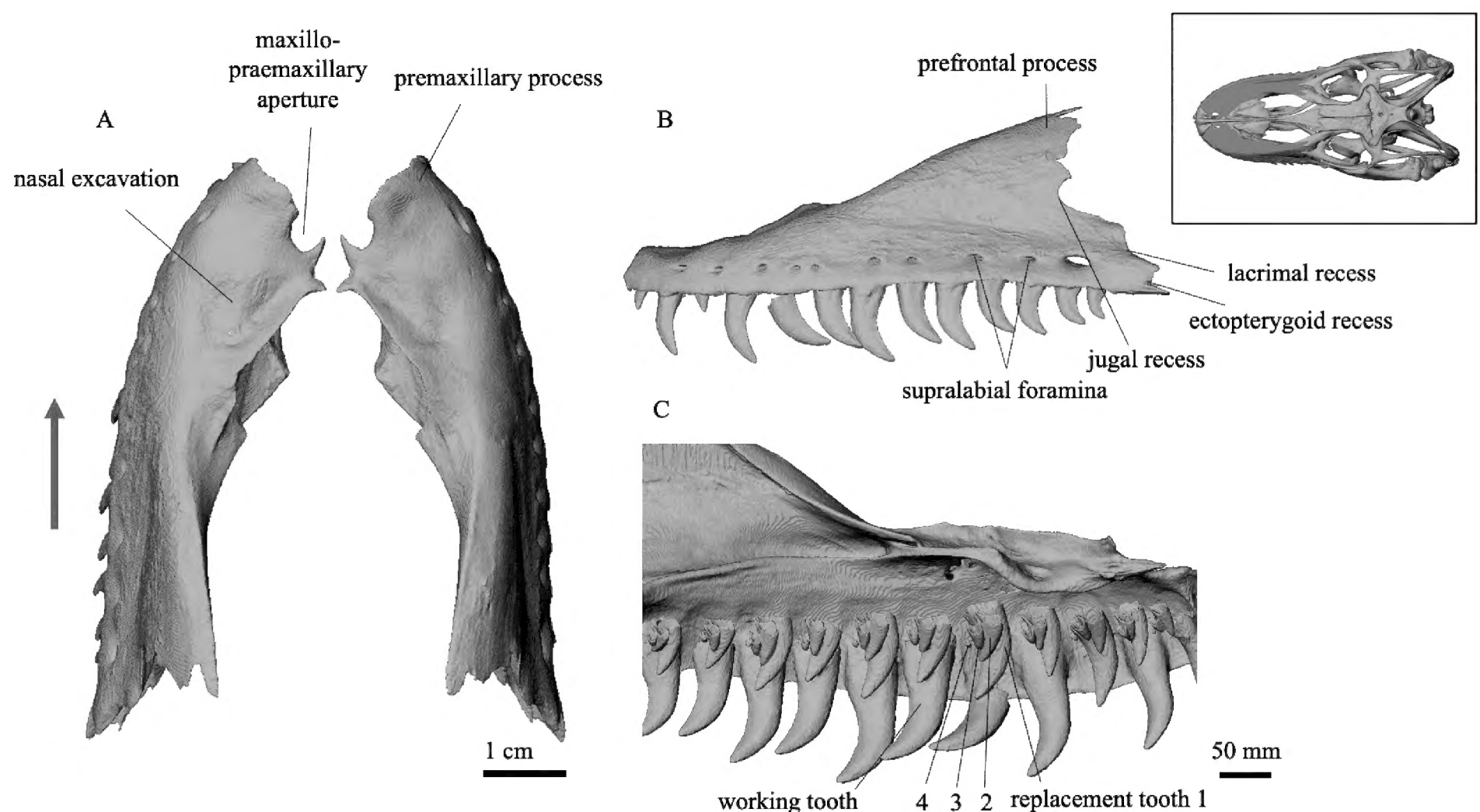

Figure 5. Maxillae. **A.** In dorsal view; **B.** Left maxilla in lateral view; **C.** Teeth and replacement teeth of the left maxilla. Arrow pointing anteriorly. Scale bars: 1 cm (**A**); 50 mm (**C**).

Posterior to the premaxillary process (Fig. 5A), which is located at the most anterior part of the maxilla, there is a notch, the maxillo-premaxillary aperture (Fig. 5A). Immediately behind it, a slight, relatively wide depression—the nasal excavation—houses the duct of the nasal vestibule (Fig. 5A, see Slaby 1979). The posterior margin of the maxilla forms the prefrontal process, which rises strongly in the posterodorsal direction. Three recesses can be iden-tified in the lower part of the posterior margin: jugal recess, lacrimal recess, and ectopterygoid recess (Fig. 5B). The maxillary tooth row accommodates positions for 13 teeth; the right maxilla in this specimen lacks one tooth, totaling twelve teeth. The teeth are sharp, laterally flattened, and posteriorly curved. Additionally, each functional tooth is accompanied by three to four smaller replacement teeth positioned directly posterior to it (Fig. 5C).

The septomaxilla is a paired, oval bone that is in contact with the maxilla anteriorly (Fig. 6). Positioned dorsally above the suture of the two septomaxillae rests the nasal process of the premaxilla. The vomer is directly ventral and adjacent to the septomaxilla. In the septomaxilla, two processes can be distinguished: the anterior and posterior processes (Fig. 6A). The dorsal surface of the septomaxilla is convex and uneven, while the ventral side is smoother and concave. A cavity on the ventral side serves as the covering for Jacobson's organ (Fig. 6B).

The nasals are fused medially in *Varanus komodoensis* (Fig. 7). The anterior process (Fig. 7A) features a very sharp, laterally compressed bifurcation that accommodates the nasal process of the premaxilla. The nasal becomes progressively wider and shallower posterolaterally. The posterior process (Fig. 7A) is three-pronged and obscures the nasal process of the frontal. Notably, the nasal and premaxilla are not fused, potentially allowing for some degree of movement between the two elements.
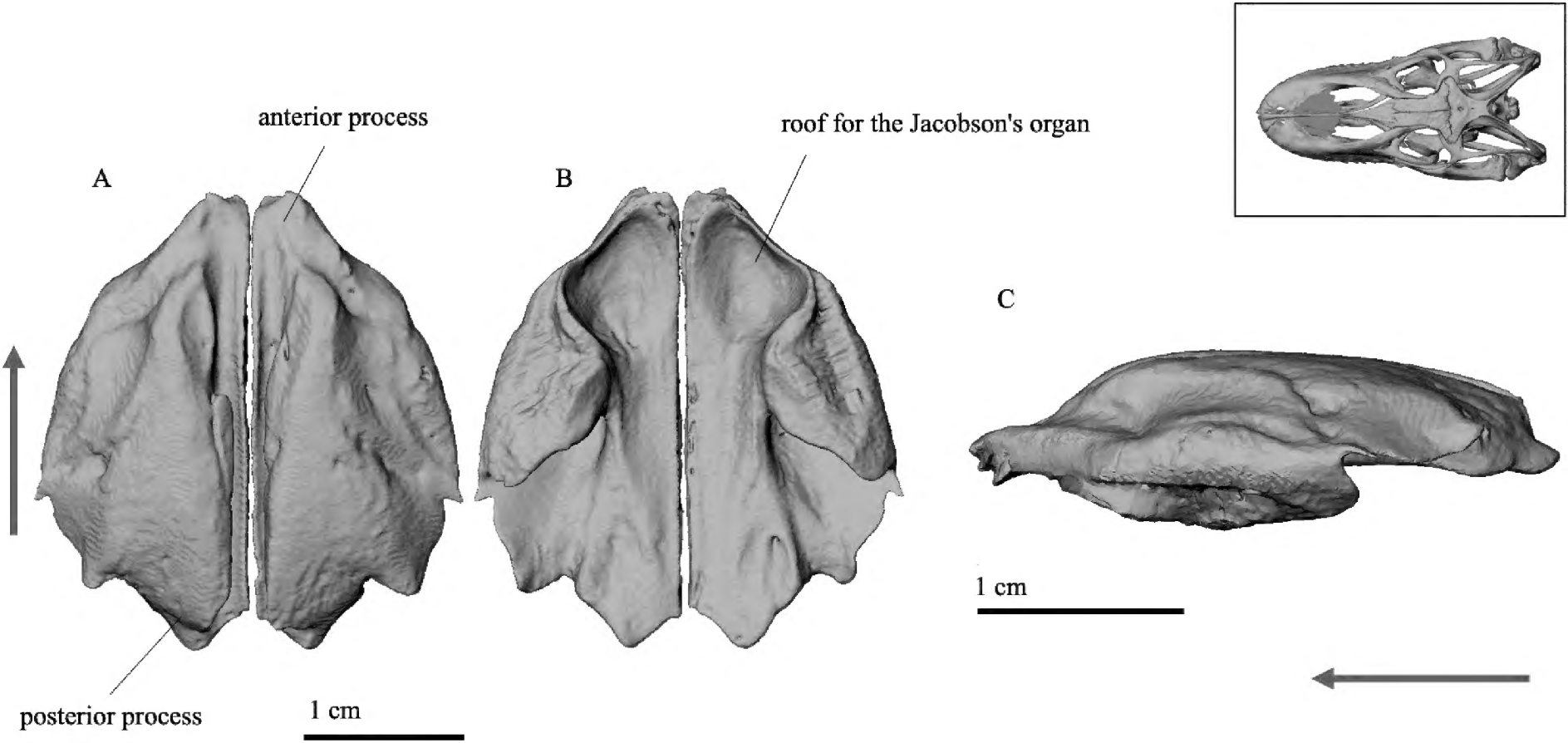
Figure 6. Septomaxilla. **A.** In dorsal; **B.** In ventral; **C.** In lateral views. Arrow pointing anteriorly. Scale bar: 1 cm.
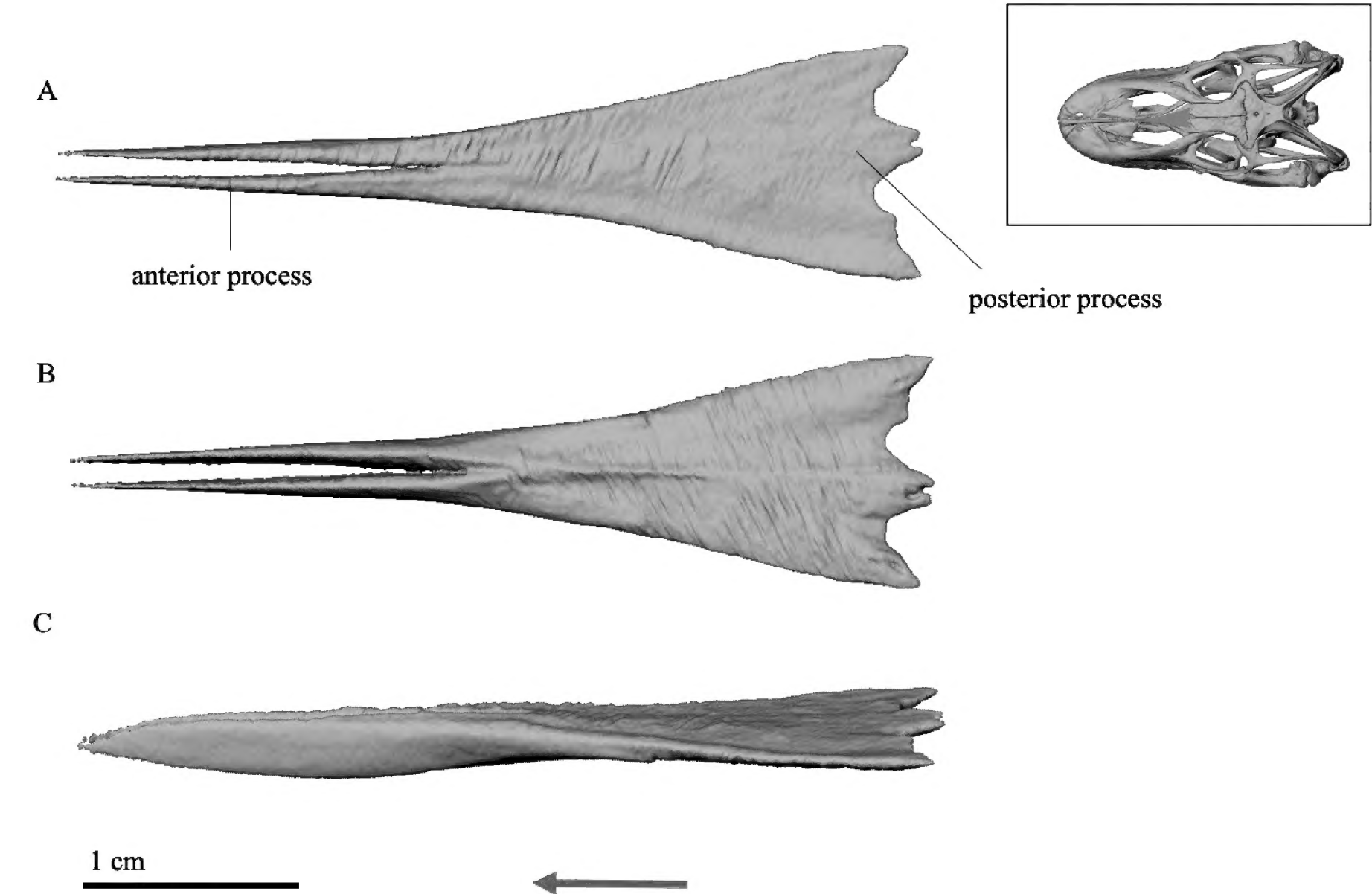
Figure 7. Nasal bone. **A.** In dorsal; **B.** In ventral; **C.** In lateral views. The nasals are fused for most of their lengths. Arrow pointing anteriorly. Scale bar: 1 cm.

The frontal is a paired bone, and together with the parietal, it forms the main support of the skull roof (Fig. 8). The anterior nasal process (Fig. 8A), which forms two sharp spikes at its anterior tip, is covered by the posterior process of the nasal. Laterally, the frontal is in contact with the prefrontal, and posteriorly, it contacts with the parietal and postorbitofrontal. The posterior end of the frontal exhibits a robust thickening and a pronounced lateral extension known as the posterolateral process (Fig. 8A). This process abuts the frontal process of the postorbitofrontal. The suture with the parietal is irregular. On the ventral side, both the right and left bony margins wrap inward, forming the lateroventral process (Fig. 8B). These processes come into contact with each other, creating the olfactory canal (Fig. 8C). The posterior end of the lateroventral process articulates with the anterior end of the orbitosphenoid.

The parietal is an unpaired, robust bone that participates with the frontal in the formation of the main structural component of the skull roof (Fig. 9). It articulates anteriorly with the frontal and postorbitofrontal, ventrally with the ascending process of the supraoccipital, and posteriorly with the supratemporal. Additionally, it is adjacent, without direct contact, to the prootic laterally, the supraoccipital ventrally, and the otooccipital posteriorly. At the anterior, irregular suture of the bone with the frontal, the parietal spreads laterally, thus forming lateral processes (Fig. 9A). Each lateral process articulates with the parietal process of the postorbitofrontal. Posteriorly, the parietal bifurcates into right and left supratemporal processes (Fig. 9A). Each supratemporal process abuts laterally on the supratemporal. The supratemporal process sharply tapers to the tip, curves downward, and reaches the most posterior part of the paroccipital process of the otooccipital. The dorsolateral face of the parietal is concave and has a sharp edge. The ventral aspect of the parietal is also concave. The parietal fossa, located

between the supratemporal processes (Fig. 9B), receives the ascending process of the supraoccipital. The parietal foramen (for the eye, Fig. 9A) is positioned medially with another smaller foramen posterior to it (Fig. 9A).

The supraorbital is a paired, narrow, tri-radiate bone (Fig. 10). The short anterior process and the long posterior process do not form sutures with neighbouring bone segments, while the inwardly and posteriorly extended medial process attaches to the prefrontal. The medial and posterior processes participate in the formation of the anterior part of the supraorbital fenestra (Fig. 10).

The prefrontals are elongated bones with three processes (Fig. 11). The slightly outwardly curved anterior process (Fig. 11C) aligns against the maxilla. The posterior orbital process (Fig. 11C) forms a relatively long suture medially with the frontal. There is also a small cusp in the center of the lateral side of the prefrontal, adjacent to the supraorbital. The ventral process (Fig. 11C) abuts the lacrimal laterally and reaches towards the palatine ventrally, although direct contact between the ventral process and the palatine is not established. The tapering anterior and ventral processes enclose a cavity between their bases (Fig. 11D). The outside of the ventral process, together with the lacrimal, forms the large lacrimal foramen (Fig. 11E) for the nasolacrimal canal.

The lacrimal is a paired, roundish bone in lateral view (Fig. 12A). It partially abuts the maxilla anteriorly and the prefrontal medially. On the ventral side of the lacrimal, the jugal and palatine lie adjacent to it, but do not form a direct suture with the lacrimal. Additionally, the lacrimal bears a small but conspicuous posterior process (Fig. 12A). This bone features two openings: the larger lacrimal foramen and smaller infraorbital foramen, respectively (Fig. 12B). The infraorbital foramen is enclosed within the lacrimal, whereas the opening of the lacrimal foramen has a gap that is closed by the prefrontal.
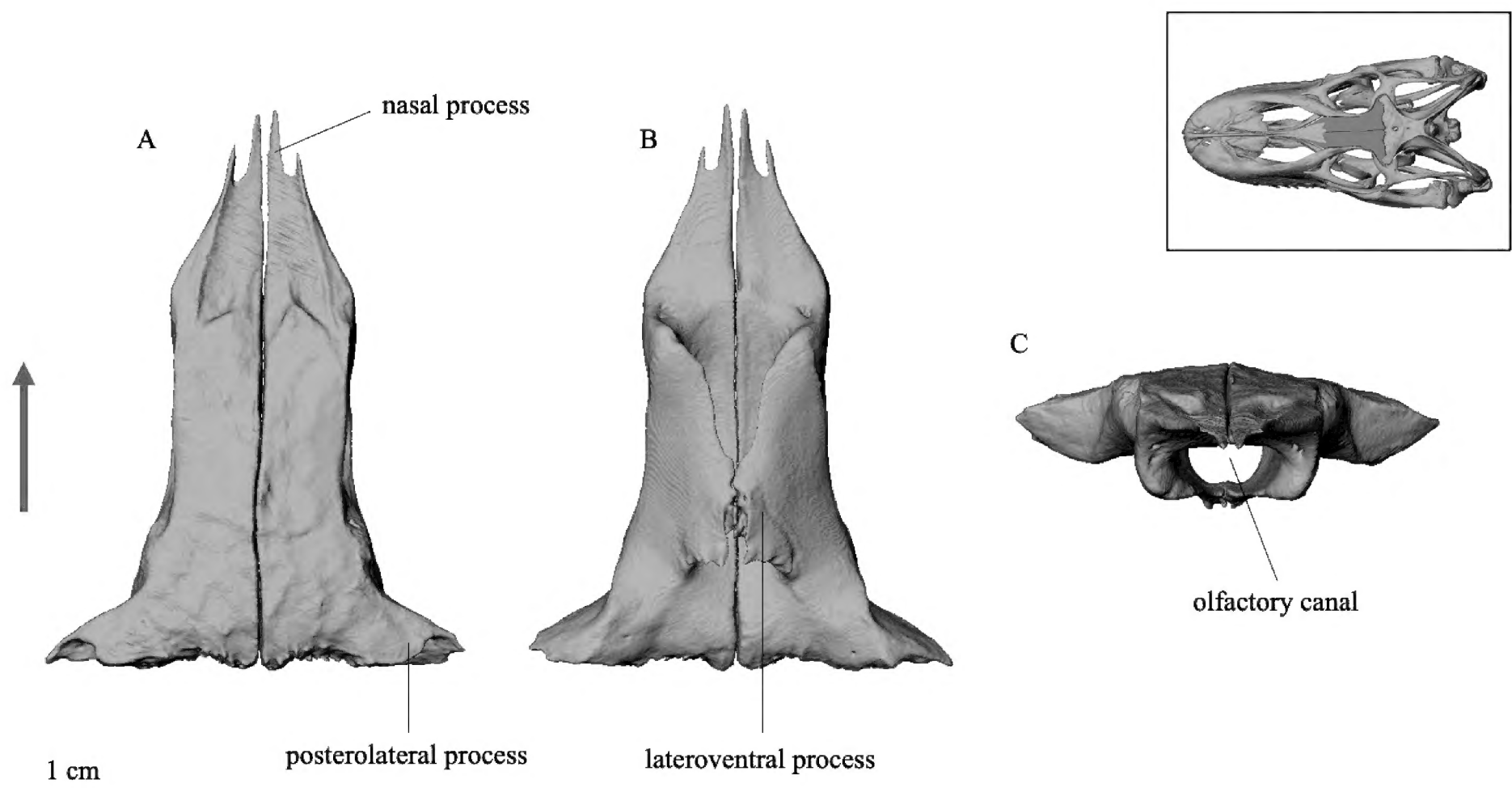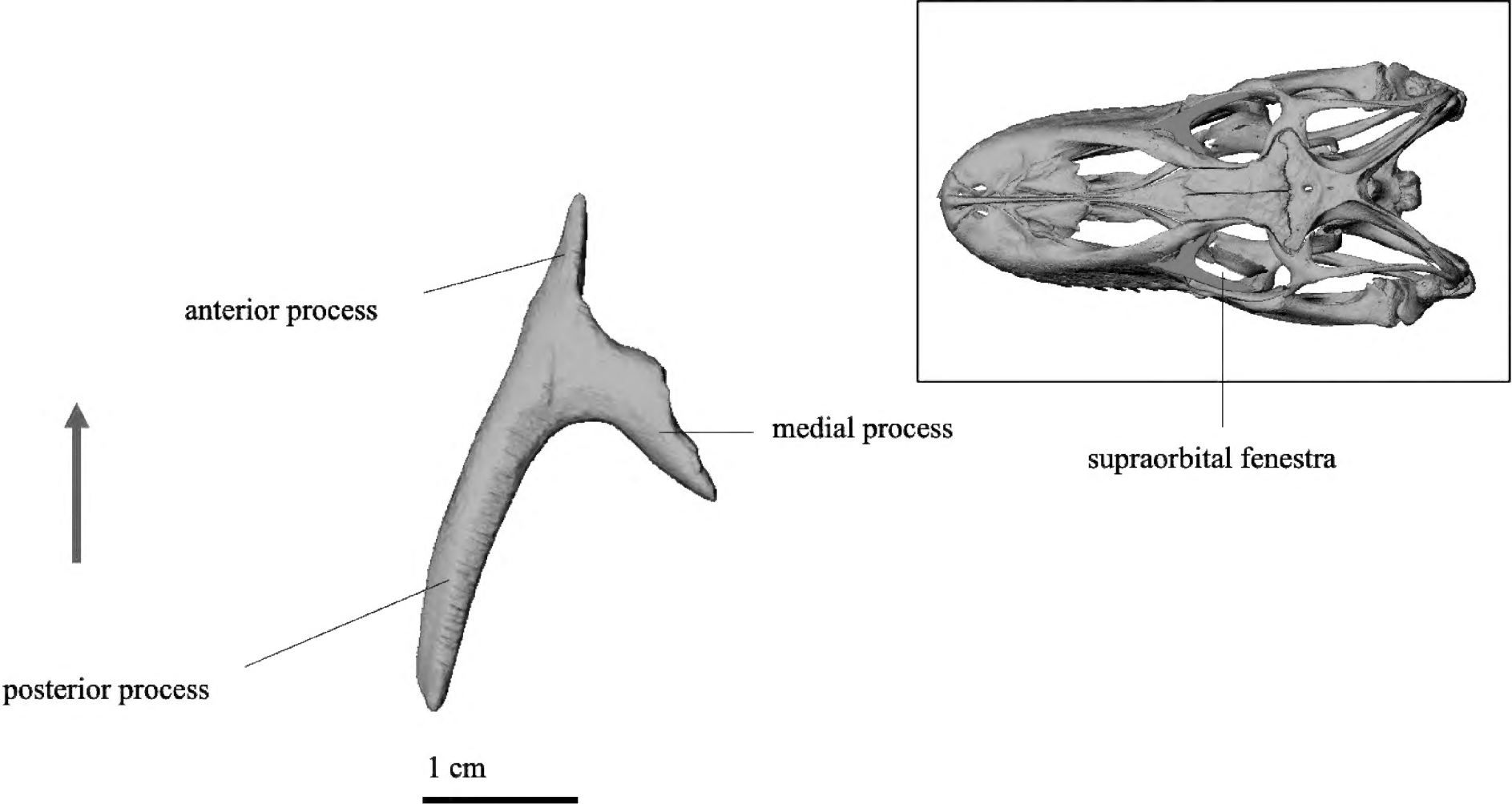

Figure 8. Frontal bones. **A.** In dorsal; **B.** In ventral; **C.** In anterior views. Arrow pointing anteriorly. Scale bar: 1 cm.
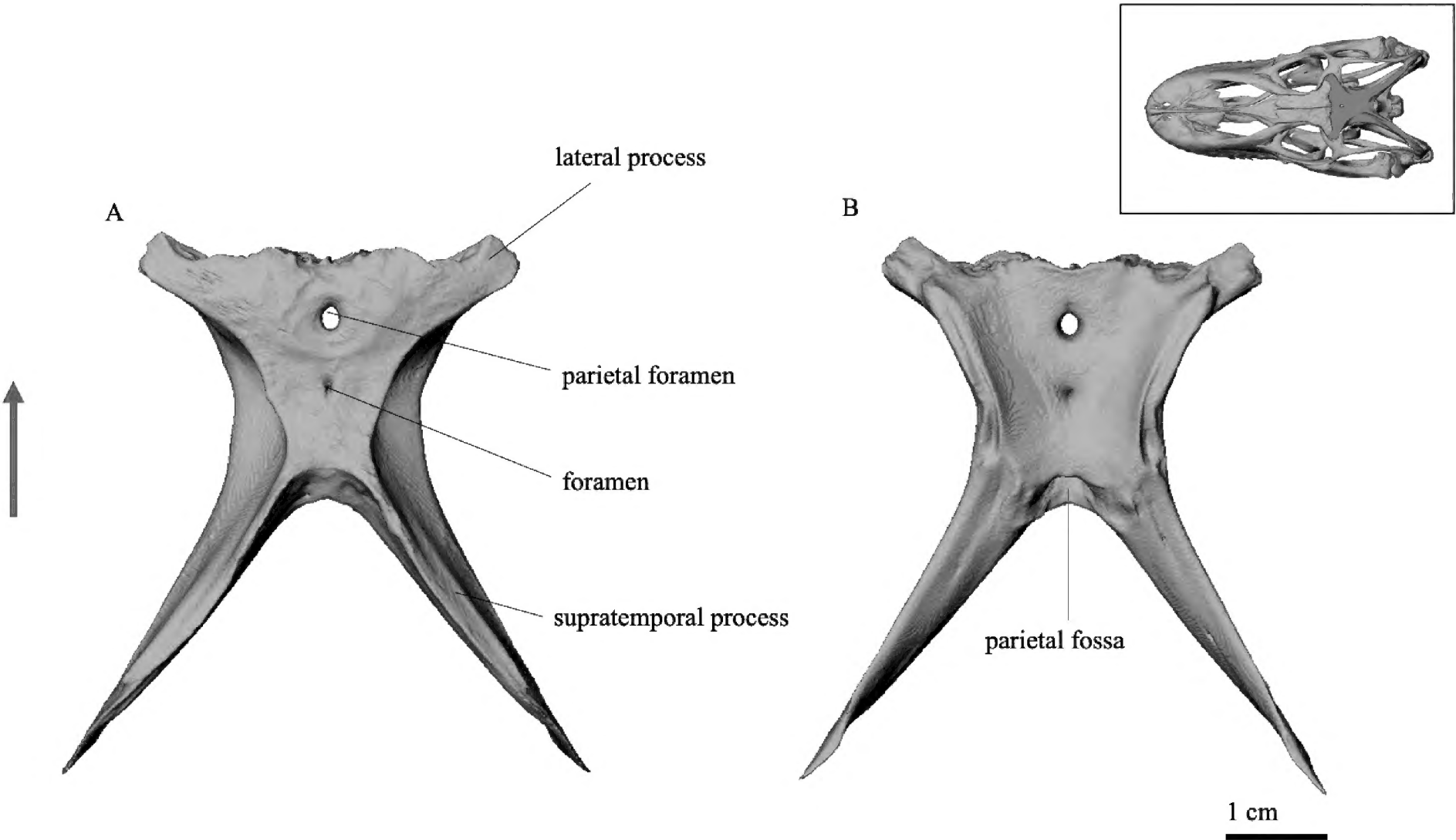
Figure 9. Parietal bone. **A.** In dorsal; **B.** In ventral views. Arrow pointing anteriorly. Scale bar: 1 cm.

Figure 10. Left supraorbital in dorsal view. Arrow pointing anteriorly. Scale bar: 1 cm.

The paired jugals are elongated, curved bones tapering distinctly towards the posterior end (Fig. 13). The posterior temporal process curves strongly dorsally and ends freely. The anterior maxillary process attaches to the maxilla and palatine and adjoins the lacrimal and ectopterygoid without tight suture. The outer surface of the jugal is concave, with relatively sharp ridges formed along the upper and lower edges of this concavity.

In *Varanus komodoensis*, the postorbital and postfrontal bones are fused, creating a singular element of com-
plex shape, known as the postorbitofrontal, characterized by four distinct processes (Fig. 14). The frontal process anteriorly (Fig. 14A) and the parietal process posteriorly (Fig. 14A) are both directed medially, with a bay between them. This bay encloses both the suture with the posterolateral process of the frontal and the lateral process of the parietal, respectively. Furthermore, the embayment contains a cavity on the dorsal side (Fig. 14A). The lateral, small orbital process (Fig. 14A) extends in the anterolateral direction and ends freely. Meanwhile,

the long, straight supratemporal process (Fig. 14A) tapers posteriorly into a sharp tip and contributes to a long suture laterally with the squamosal. This conjunction of the supratemporal process and the opposing squamosal process creates the supratemporal bridge (Fig. 14C). Additionally, pairs of small foramina are present at the base of the parietal process, both dorsally and ventrally (Fig. 14A, B).

The squamosal is a paired, narrow, laterally flattened, and sickle-shaped bone (Fig. 15). It forms a long suture anteromedially with the supratemporal process of the postorbitofrontal and contributes to the formation of the supratemporal bridge (Fig. 15C). The posterior part of the squamosal sharply curves ventrally, bordering the supratemporal medially and the quadrate ventrally. Direct bone to bone contact, however, between the squamosal and the quadrate is not established in the CT data and presumably filled with other tissue types (articulation). The outer surface of the squamosal is convex (Fig. 15A), the inner surface is concave (Fig. 15B).
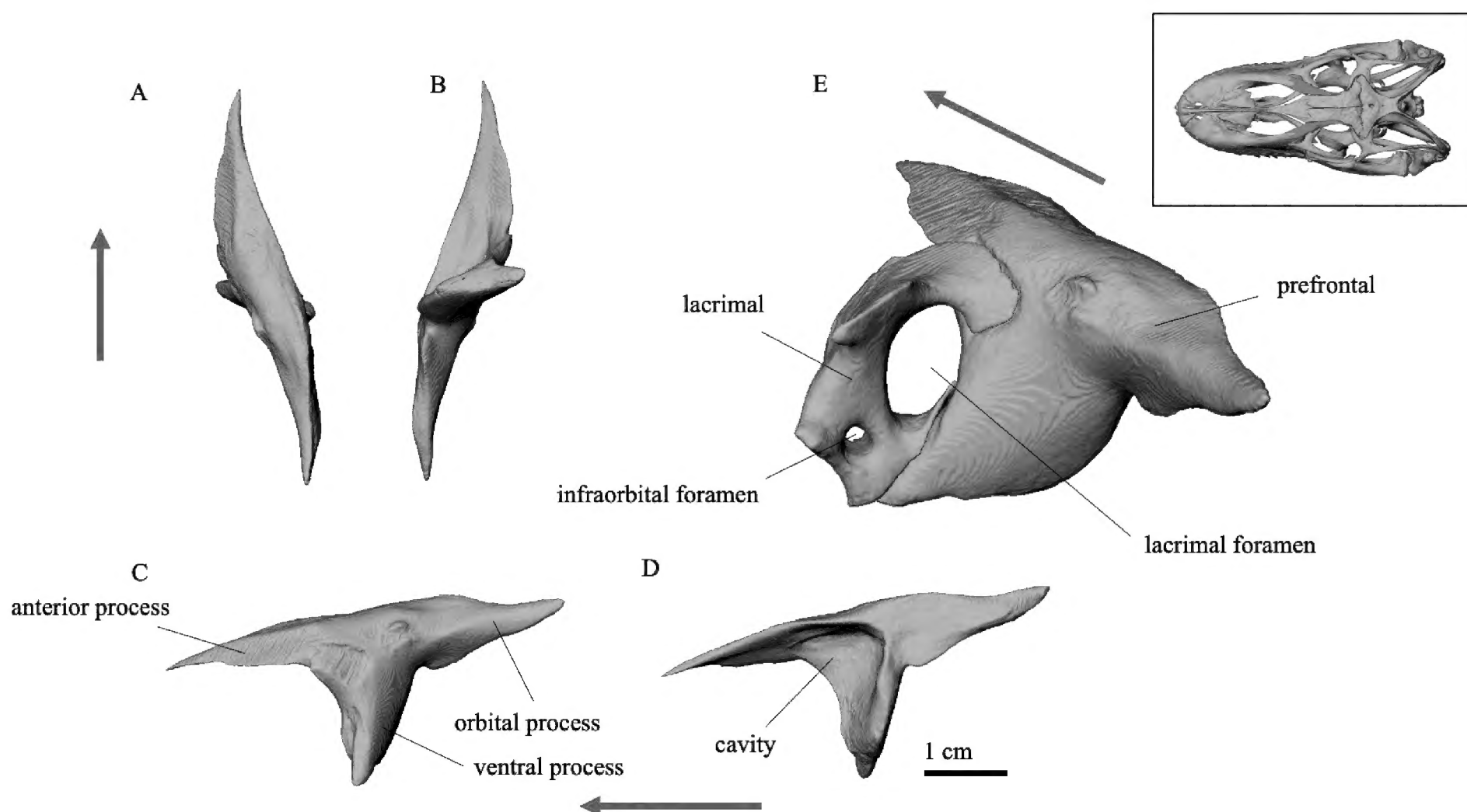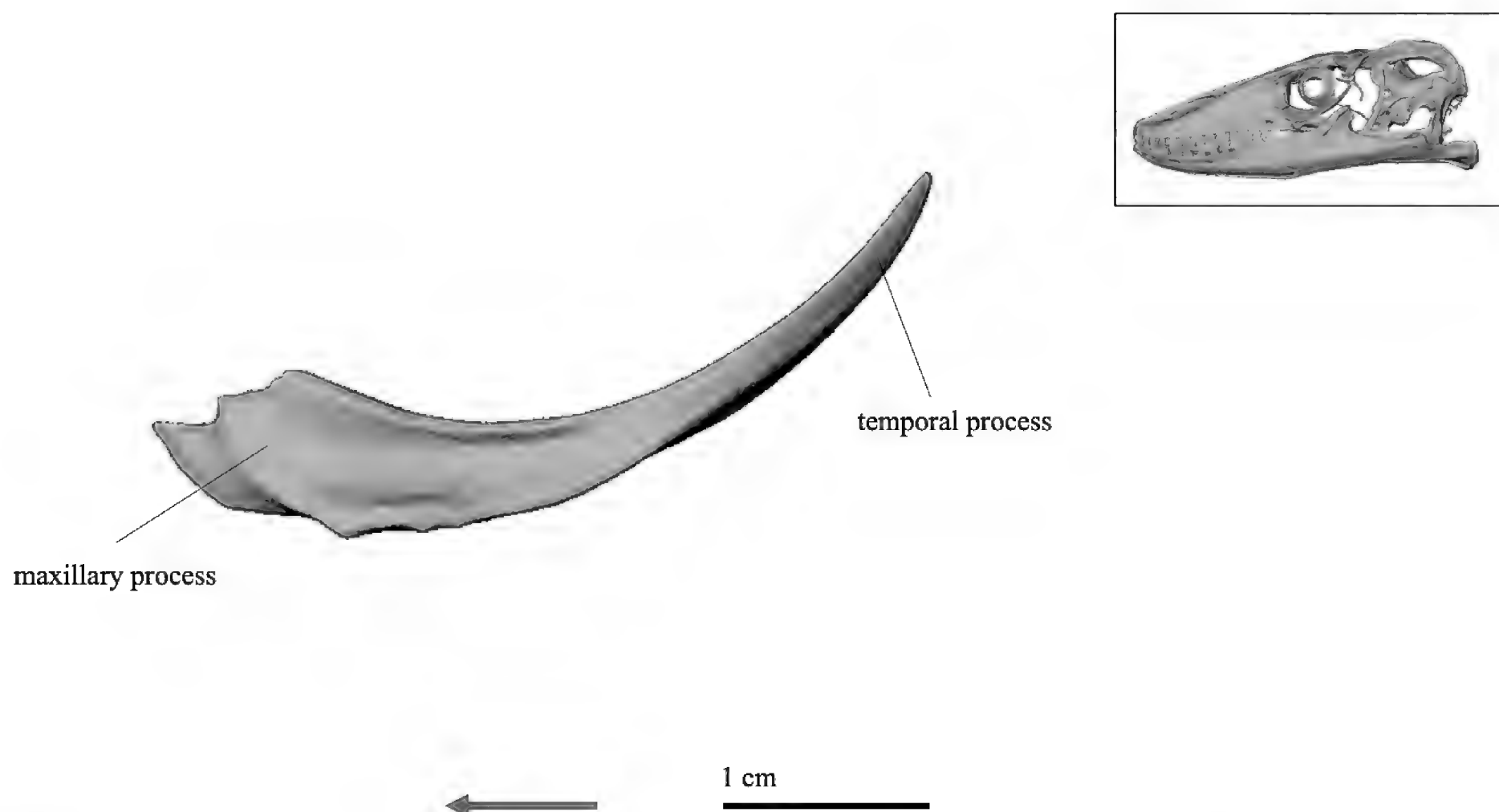

Figure 11. Prefrontal bones. **A.** Left prefrontal in dorsal; **B.** In ventral; **C.** In lateral views; **D.** Right prefrontal in medial view; **E.** Lacrimal and prefrontal in posterolateral view with lacrimal foramina. Arrow indicates anterior direction. Scale bar: 1 cm (**A, B, C, D**).
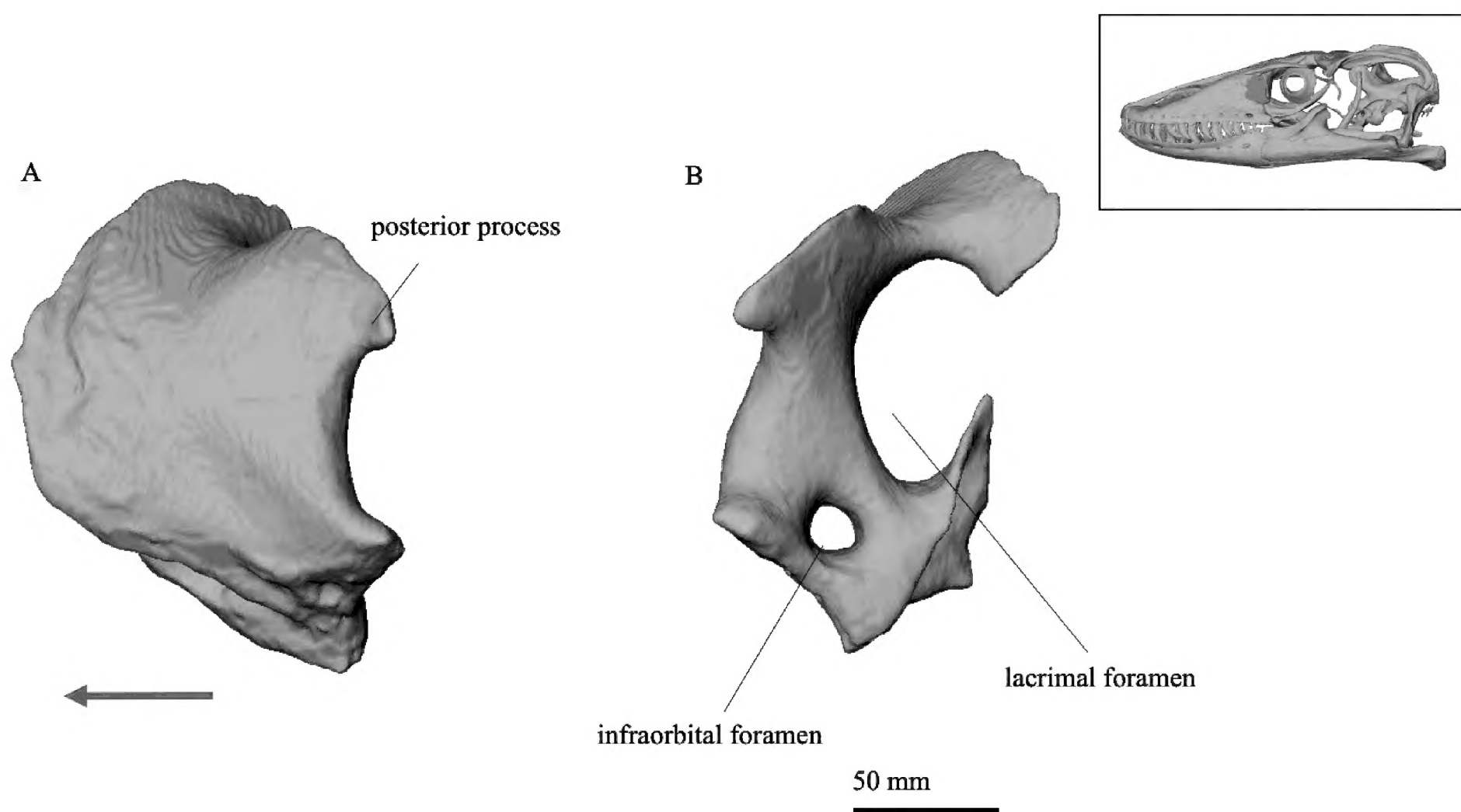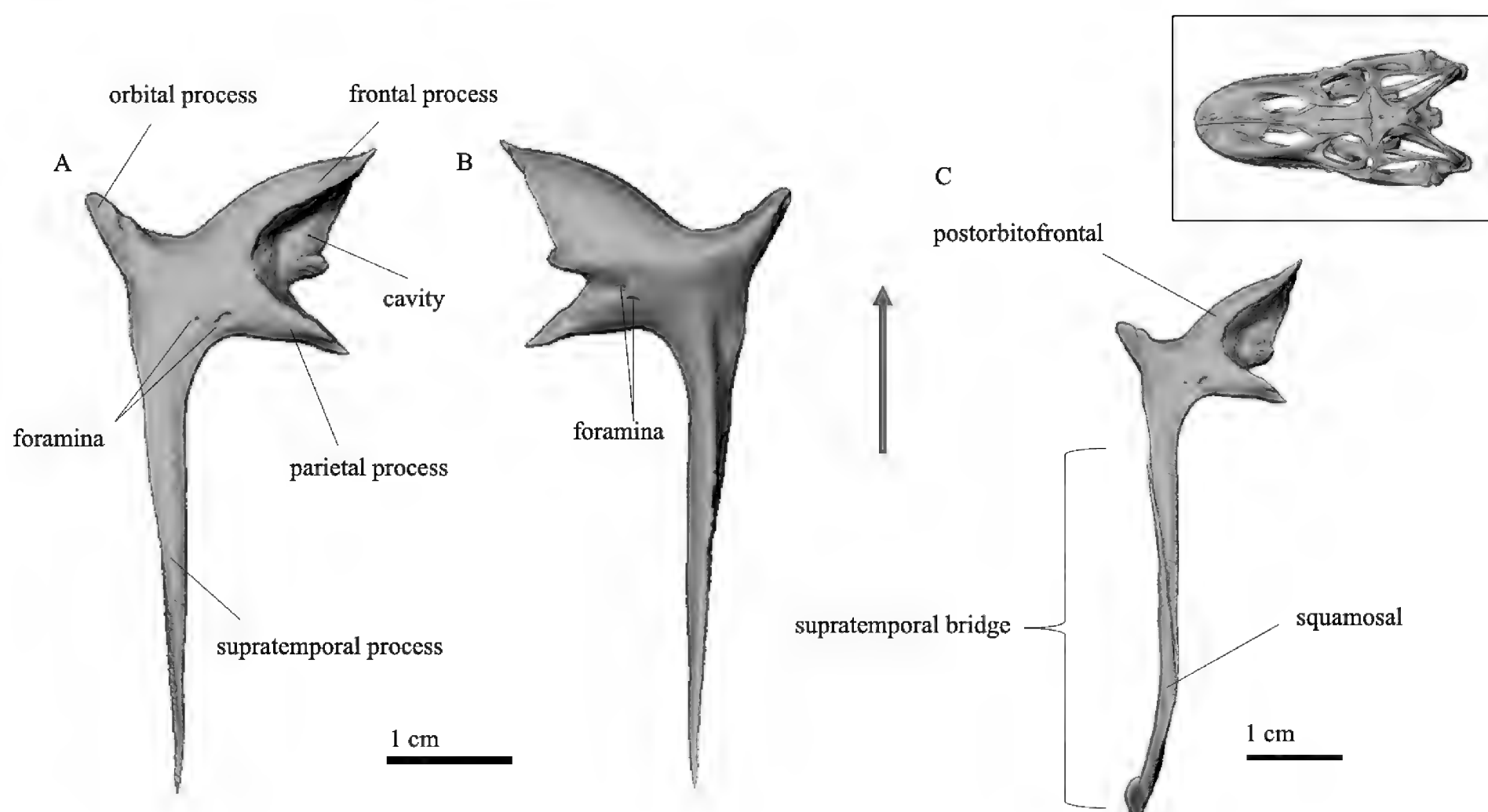

Figure 12. Lacrimal. **A.** Left lacrimal in lateral; **B.** Same in posterior views. Arrow pointing anteriad. Scale bar: 50 mm.

Figure 13. Left jugal in lateral view. Arrow pointing anteriad. Scale bar: 1 cm.
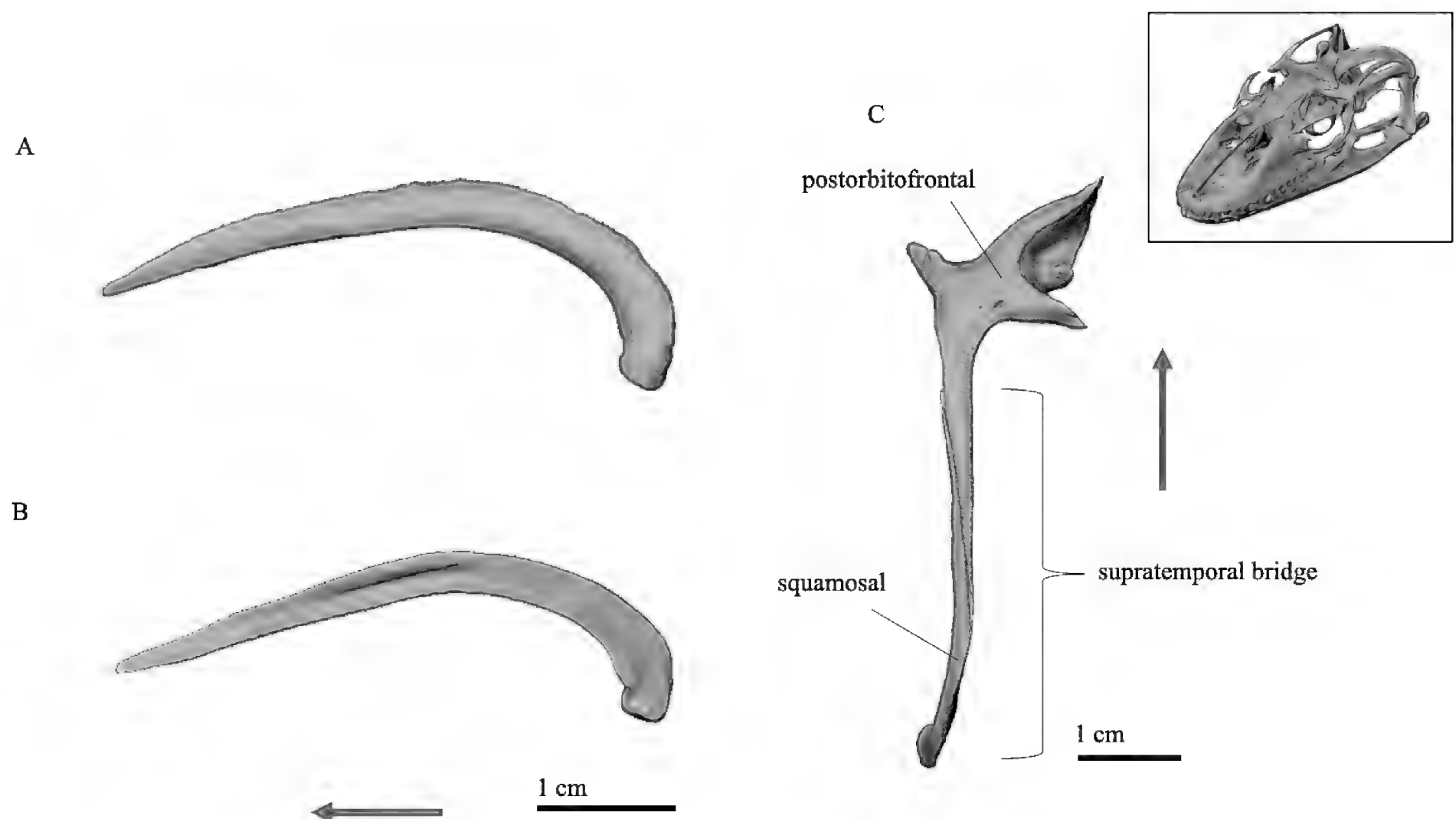

Figure 14. Postorbitofrontal. **A.** Left postorbitofrontal in dorsal; **B.** In ventral views; **C.** Formation of the supratemporal bridge by the postorbitofrontal and squamosal. Arrow pointing anteriad. Scale bars: 1 cm.

The supratemporal, a paired bone with lateral compressed, establishes a long suture with the supratemporal process of the parietal (Fig. 16). It articulates laterally with the squamosal, ventrally with the quadrate, and medially with the paroccipital process of the otooccpital. Its anterior margin is acuminate, whereas the posterior margin is rounded. In lateral view, the supratemporal strongly curves downward posteriorly (Fig. 16B).

The quadrate is a paired, vertically elongate bone (Fig. 17). Its upper extremity forms the cephalic condyle, while the lower extremity forms the mandibular condyle and the pterygoid condyle (Fig. 17B). The cephalic condyle articulates with the supratemporal and is adjacent to the squamosal and paroccipital process of the otooccipital without direct contact. A small, oval-shaped, flattened intercalar element is located between the cephalic condyle and the paroccipital process of the otooccipital (Fig. 17E). The mandibular condyle articulates medially with the quadrate process of the pterygoid and ventrally with the articular. On the inner face of the quadrate, a sulcus with a sharp edge is discernible (Fig. 17A).

Figure 15. Squamosal. **A.** Left squamosal in lateral view; **B.** Right squamosal in medial view; **C.** Supratemporal bridge through contribution of the postorbitofrontal and the squamosal. Arrow pointing anteriad. Scale bars: 1 cm.
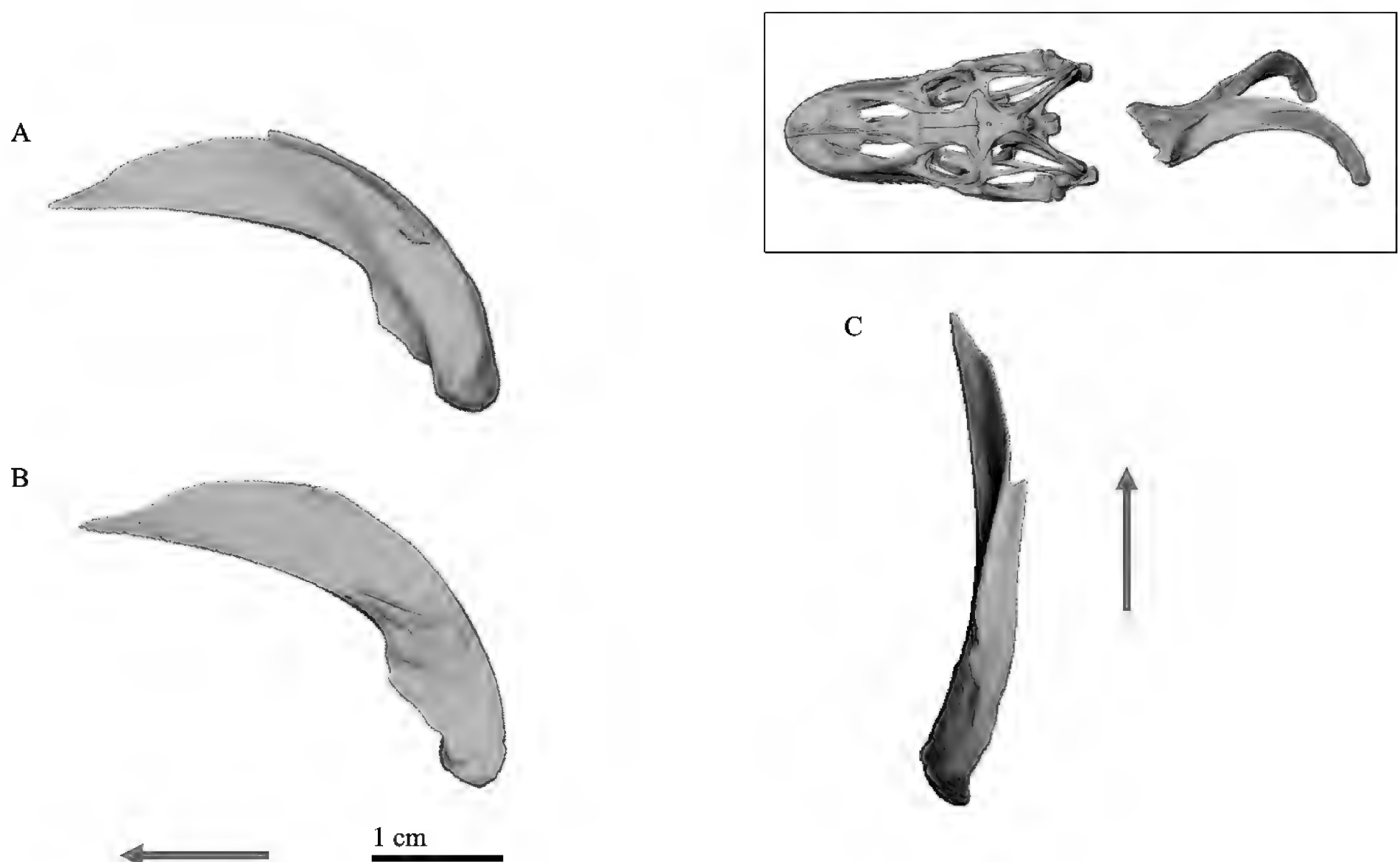

Figure 16. Supratemporal. **A.** Left supratemporal in lateral view; **B.** Right supratemporal in medial view; **C.** Left supratemporal in dorsal view. Arrows point anteriad. Scale bar: 1 cm.

The sclerotic ring of *Varanus komodoensis* consists of 15 fused plates (Fig. 18).

The columella of *Varanus komodoensis* is rod-shaped and extends outward (Fig. 19A). The anterior part of the columella enters the oval window (fenestra ovalis) of the paroccipital process of the otooccipital. Positioned immediately posterior to the columella is the extracolumella, which supports the tympanic membrane (Fig. 19A). The anterior part of the extracolumella curves in the ventrolateral direction, while its posterior part bifurcates (Fig. 19B).
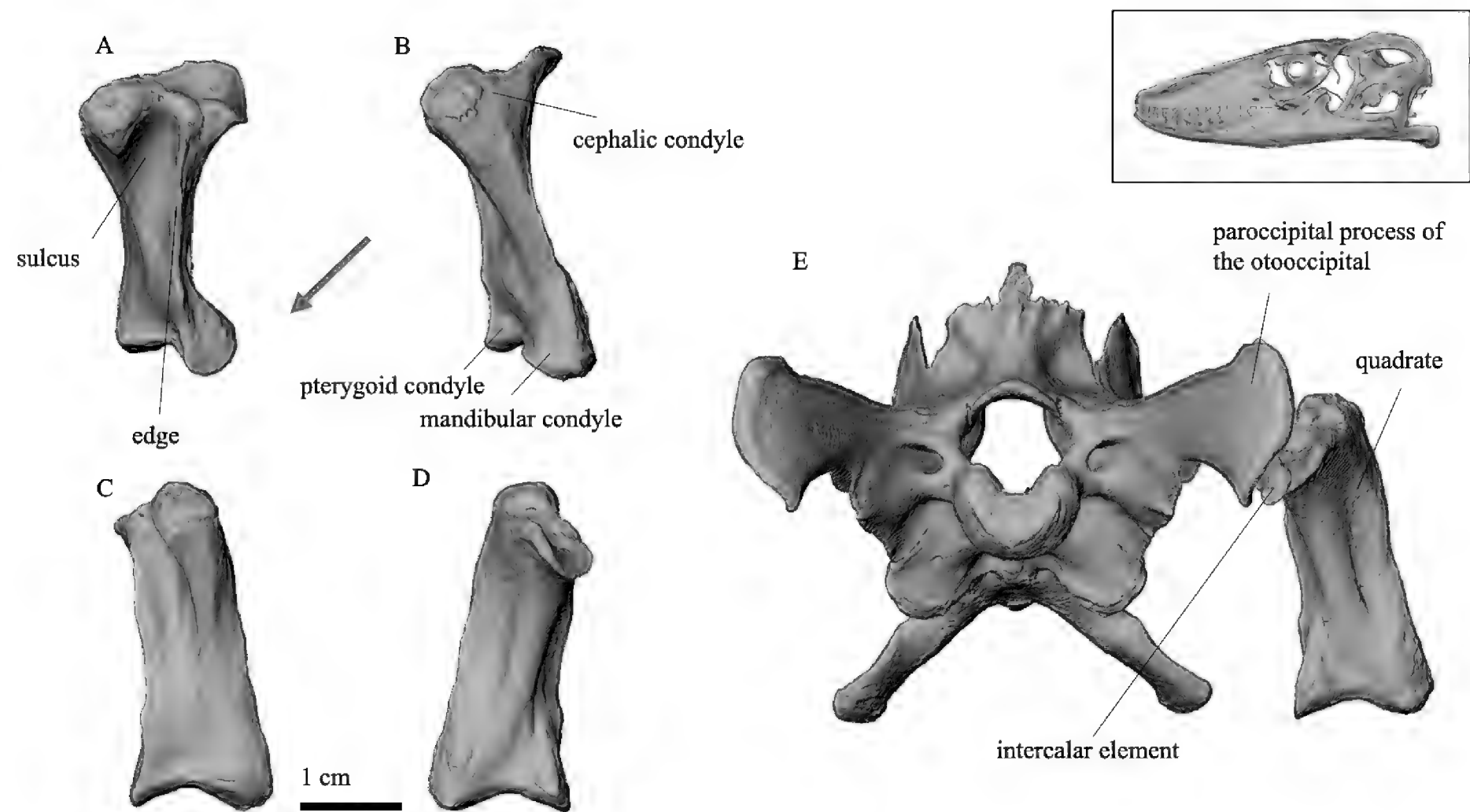
Figure 17. Quadrate. **A.** Right quadrate in anteromedial view; **B.** Left quadrate in anterolateral view; **C.** Left quadrate in anterior view; **D.** Right quadrate in posterior view; **E.** Intercalar element. Arrow pointing anteriad. Scale bar: 1 cm (**A, B, C, D**).
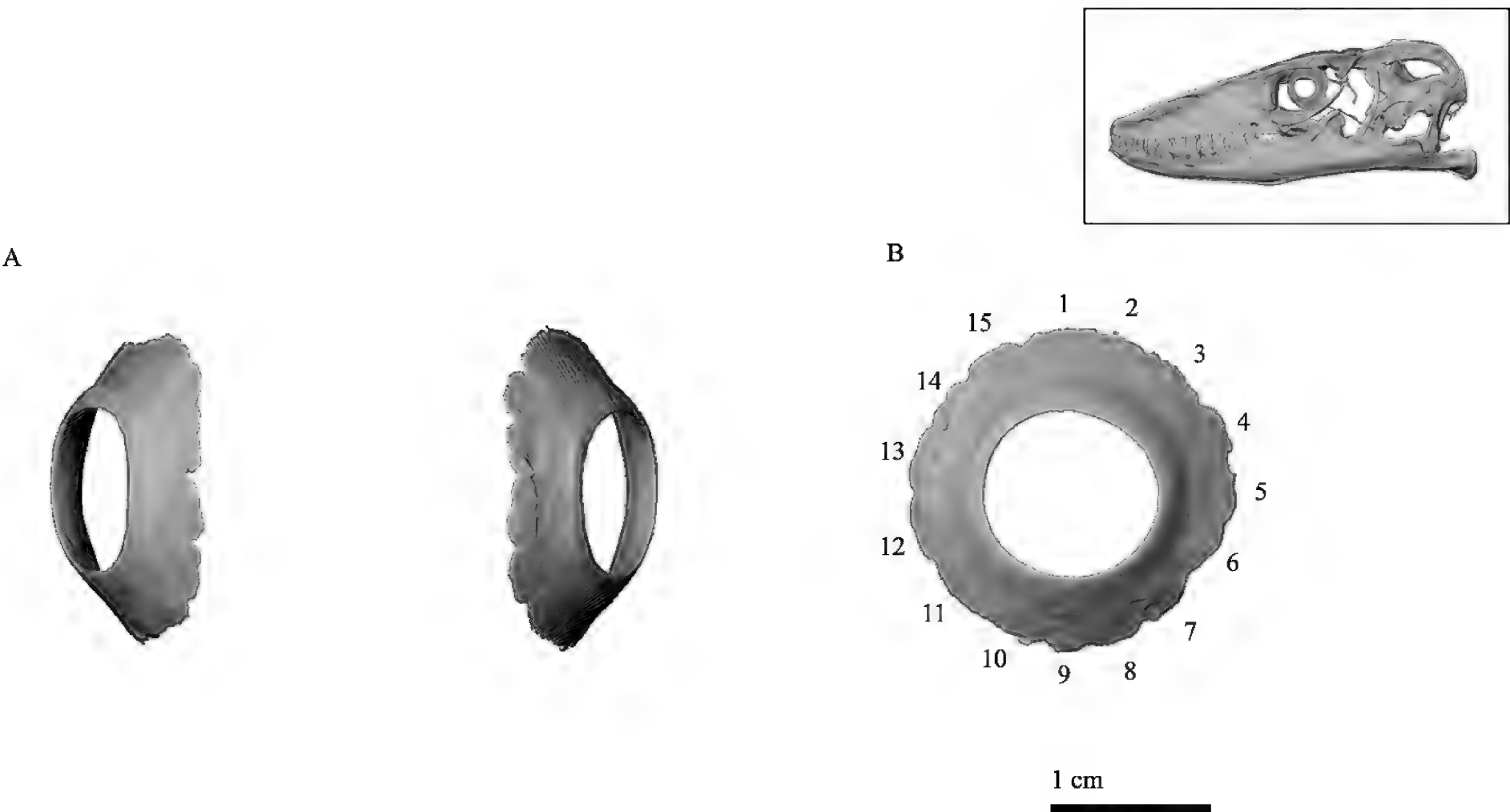
Figure 18. Sclerotic ring. **A.** Right and left sclerotic ring in anterior view; **B.** Left sclerotic ring in lateral view with plate number. Scale bar: 1 cm.

The small, paired orbitosphenoid does not articulate directly with any other bone (Fig. 20). The anterior part of the orbitosphenoid is sickle-shaped with a pointed tip posteriorly. The posterior part of the orbitosphenoid curves ventrally and medially. In the image, the orbitosphenoids appear to fuse medially in one section (Fig. 20B), but this is likely a CT visualization artifact of the two very close elements.

Palate

The paired vomer is an elongate bone with a complicated structure (Fig. 21). It makes contact with the maxilla anteriorly and is dorsally covered by the septomaxilla, although direct contact is not formed. The two vomers are directly adjacent, but do not fuse (Fig. 21A, B). Both the flattened anterior process and the posterior process

taper to form pointed tips (Fig. 21A). The posterior process features a lateral cavity that receives the vomerine process of the palatine (Fig. 21C). A deep groove on the dorsal face of the vomer extends through a substantial portion of the element (Fig. 21A). The groove is bordered medially and laterally by longitudinal ridges (Fig. 21A), with the outer ridge higher and curved inward. Additionally, an oval-shaped foramen is present at the inner ridge (Fig. 21C). At the base of the anterior process, a small dorsally projecting process, with no contact with other bone segments, is present (Fig. 21C). This process extends into the ventral cavity of the septomaxilla, forming a ventral insertion into the cavity of Jacobson's organ. Ventrally, there is also a groove with inner and outer ridges, respectively (Fig. 21B). The

incisive foramen, serving as an opening for Jacobson's organ, is located at the ventral side of the anterior process (Fig. 21D).

The paired palatine bone consists of several processes (Fig. 22). The anterior, long vomerine process (Fig. 22A) tapers anteriorly and curves slightly medially. It is received by the cavity at the vomerine posterior process. The posterior, laterally elongated maxillary process (Fig. 22A) is adjacent to the maxilla, jugal, ectopterygoid, prefrontal, and lacrimal, although it does not form direct sutures with the last two bones. The posterior, internal pterygoid process (Fig. 22A) bifurcates and attaches to the pterygoid. At the indentation between the maxillary and pterygoid processes, there is also a large opening, the maxillo-palatine foramen (Fig. 22C).
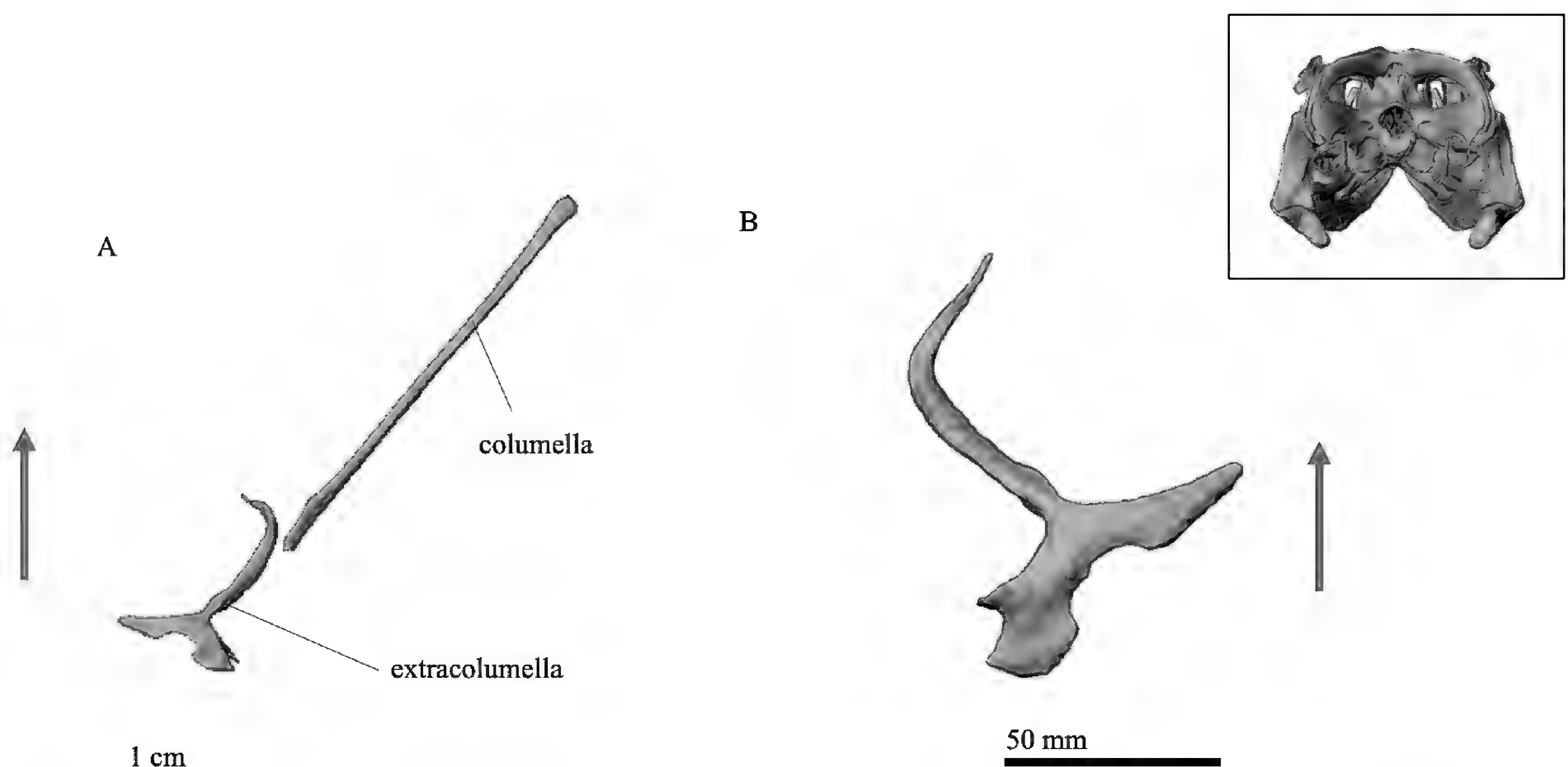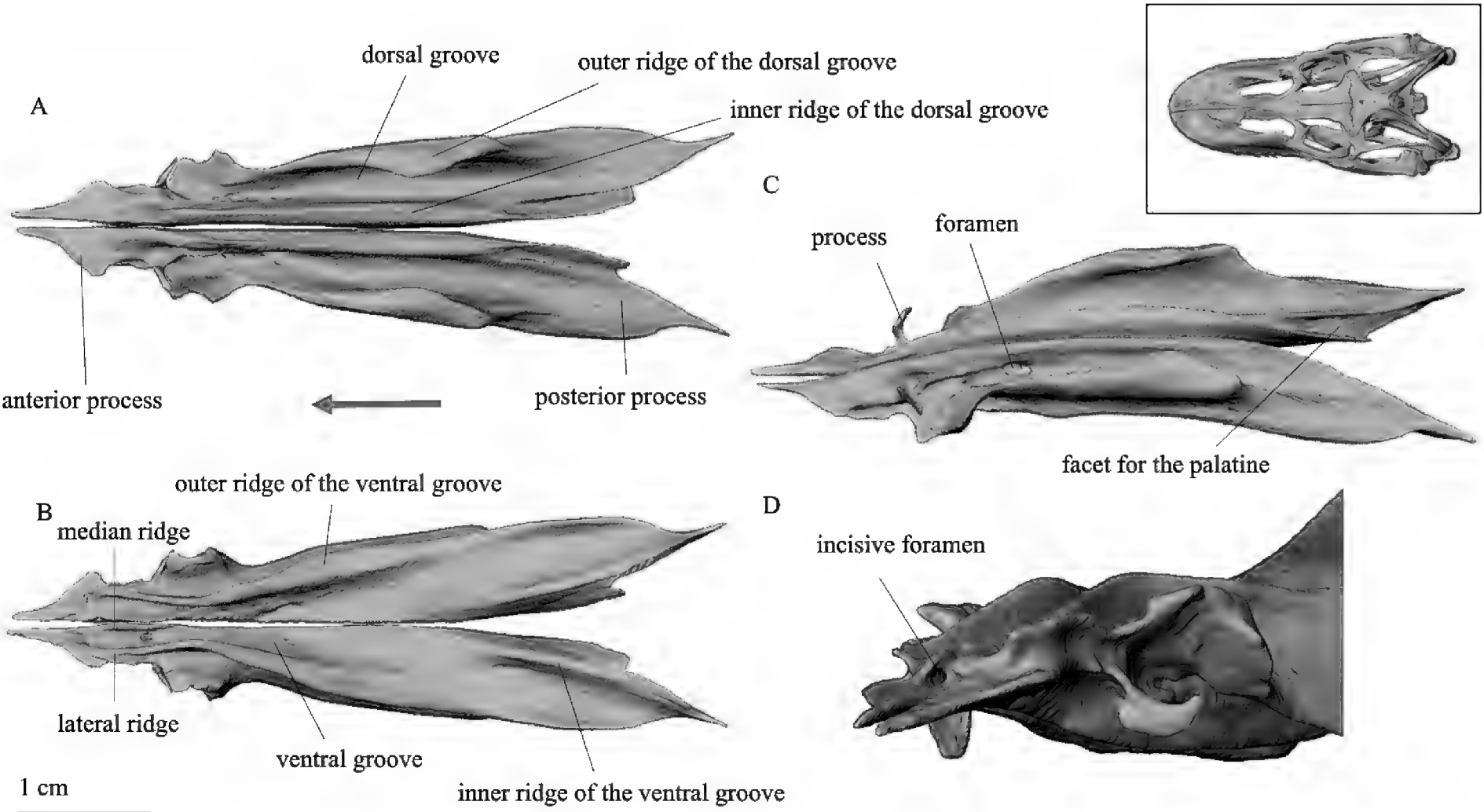

Figure 19. Columella. **A.** Left columella and left extracolumella in dorsal view; **B.** Left extracolumella in ventral view. Arrow pointing anteriad. Scale bars: 1 cm (**A**); 50 mm (**B**).
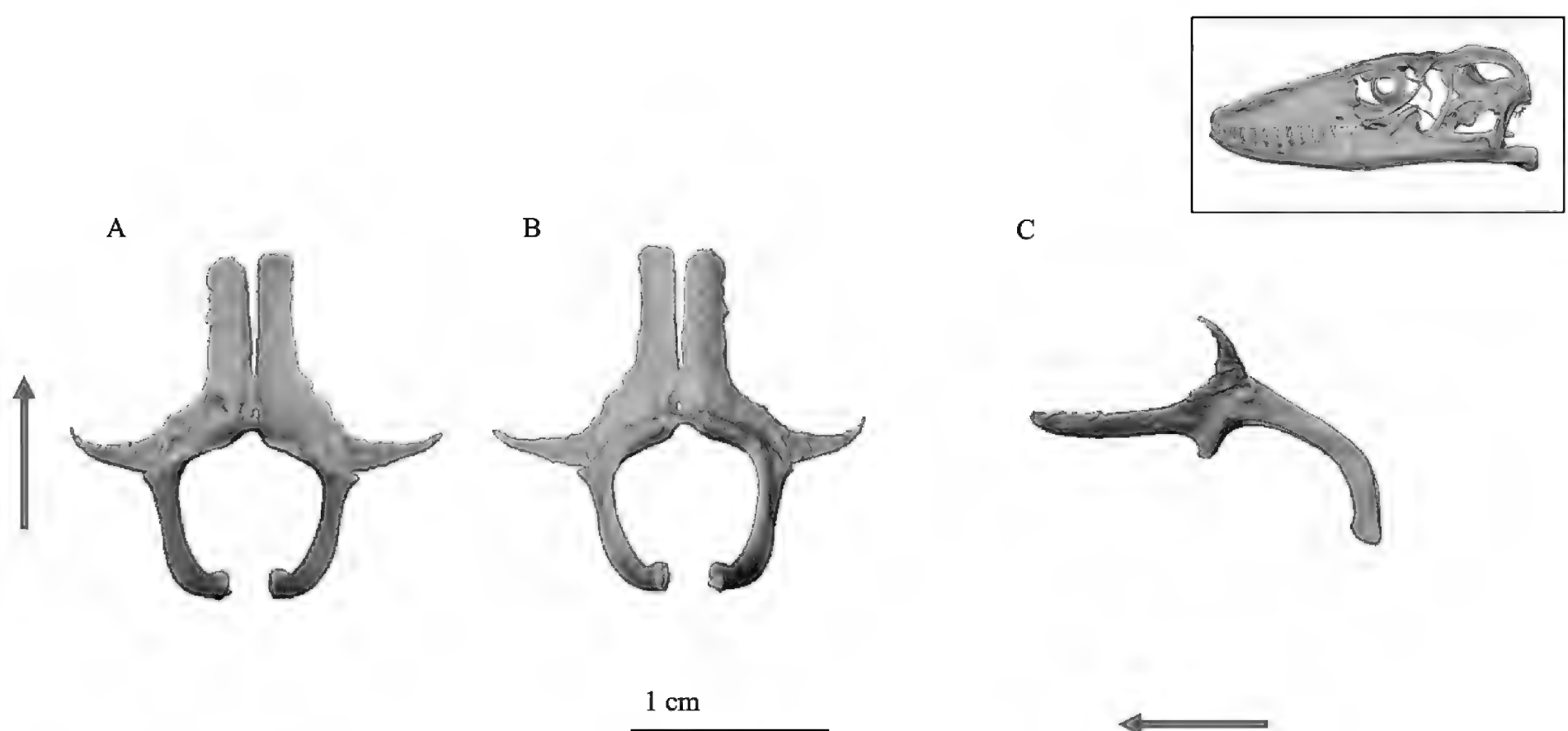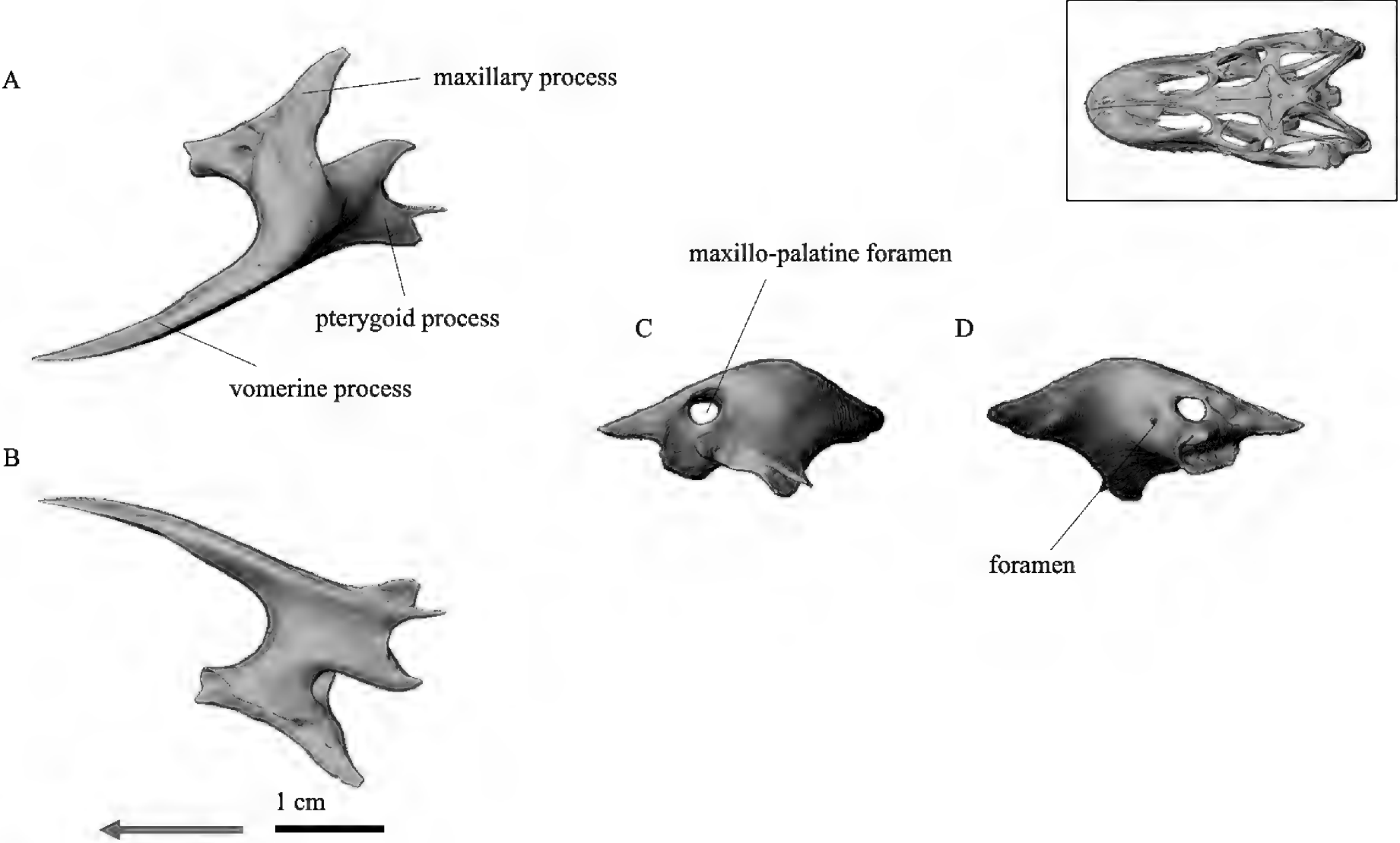

Figure 20. Orbitosphenoid. **A.** In dorsal; **B.** In ventral; **C.** In lateral views. Arrow pointing anteriad. Scale bar: 1 cm.

Figure 21. Vomer. **A.** In dorsal; **B.** In ventral; **C.** In dorsolateral views; **D.** Anterior part of the ventral side of the vomer in antero-lateral view. Arrow pointing anteriad. Scale bar: 1 cm (**A, B, C**).

Figure 22. Palatine. **A.** Right palatine in dorsal view; **B.** Right palatine in ventral view; **C.** Left palatine in posterior view; **D.** Left palatine in anterior view. Arrow pointing anteriad. Scale bar: 1 cm.

The ectopterygoid is a paired, small bone featuring one process at the anterior end and two processes at the posterior end (Fig. 23). The anterior maxillary process (Fig. 23A) makes contact with the palatine dorsally and with the maxilla ventrally. A bifurcation is present between the dorsal pterygoid process and ventral pterygoid process (Fig. 23A); it receives the ectopterygoid process of the pterygoid. Dorsally to the ectopterytgoid, the jugal is in close proximity but does not form a suture.

The pterygoid is a long bone that gives rise to three processes (Fig. 24). The anterior, short, laterally directed ectopterygoid process (Fig. 24A) is received between the dorsal pterygoid process and the ventral pterygoid process of the ectopterygoid. The anterior, medial, and broad

palatine process (Fig. 24A) bears two small spines at its anterior margin and supports the pterygoid process of the palatine. The posterior, stylus-like quadrate process (Fig. 24A) curves slightly laterally. It borders the basipterygoid process of the basisphenoid anteromedially without direct contact and forms a suture with the quadrate posterolaterally. At the origin of the quadrate process, a dorsally located fossa columella comes in contact with the epipter-ygoid (Fig. 24A). Immediately posterior to the fossa columella, a short groove is present (Fig. 24A), while a deep, longer groove is present on the ventral side of the quadrate process (Fig. 24B). At the junction of the palatine process and quadrate process, the small basisphenoid tuberculum is located laterally (Fig. 24B). A ventral cavity is part of the bay formed between the ectopterygoid and palatine processes (Fig. 24B).
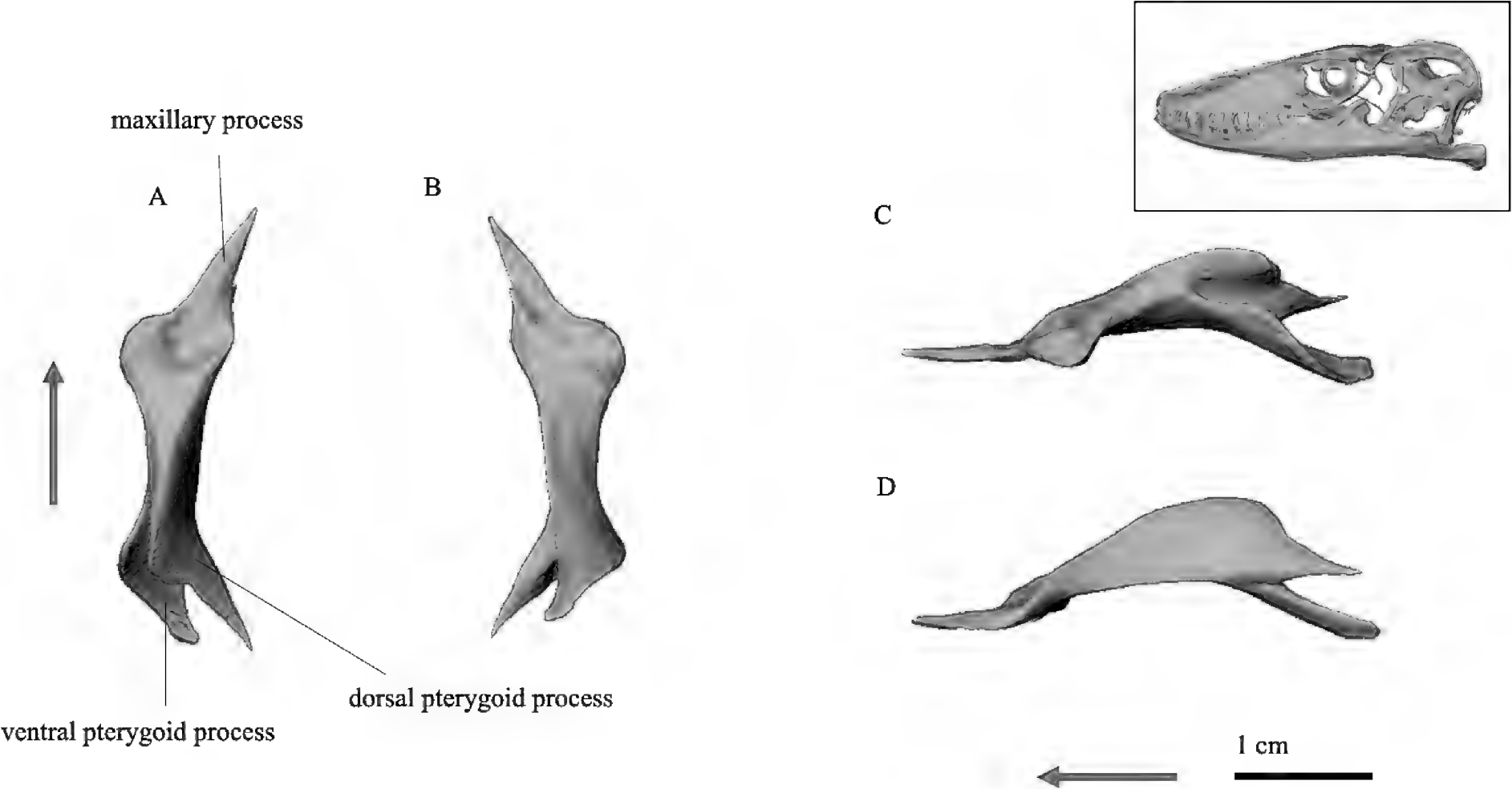
Figure 23. Ectopterygoid. **A.** Left ectopterygoid in dorsal; **B.** In ventral; **C.** In lateral views; **D.** Right ectopterygoid in medial view. Arrow pointing anteriad. Scale bar: 1 cm.
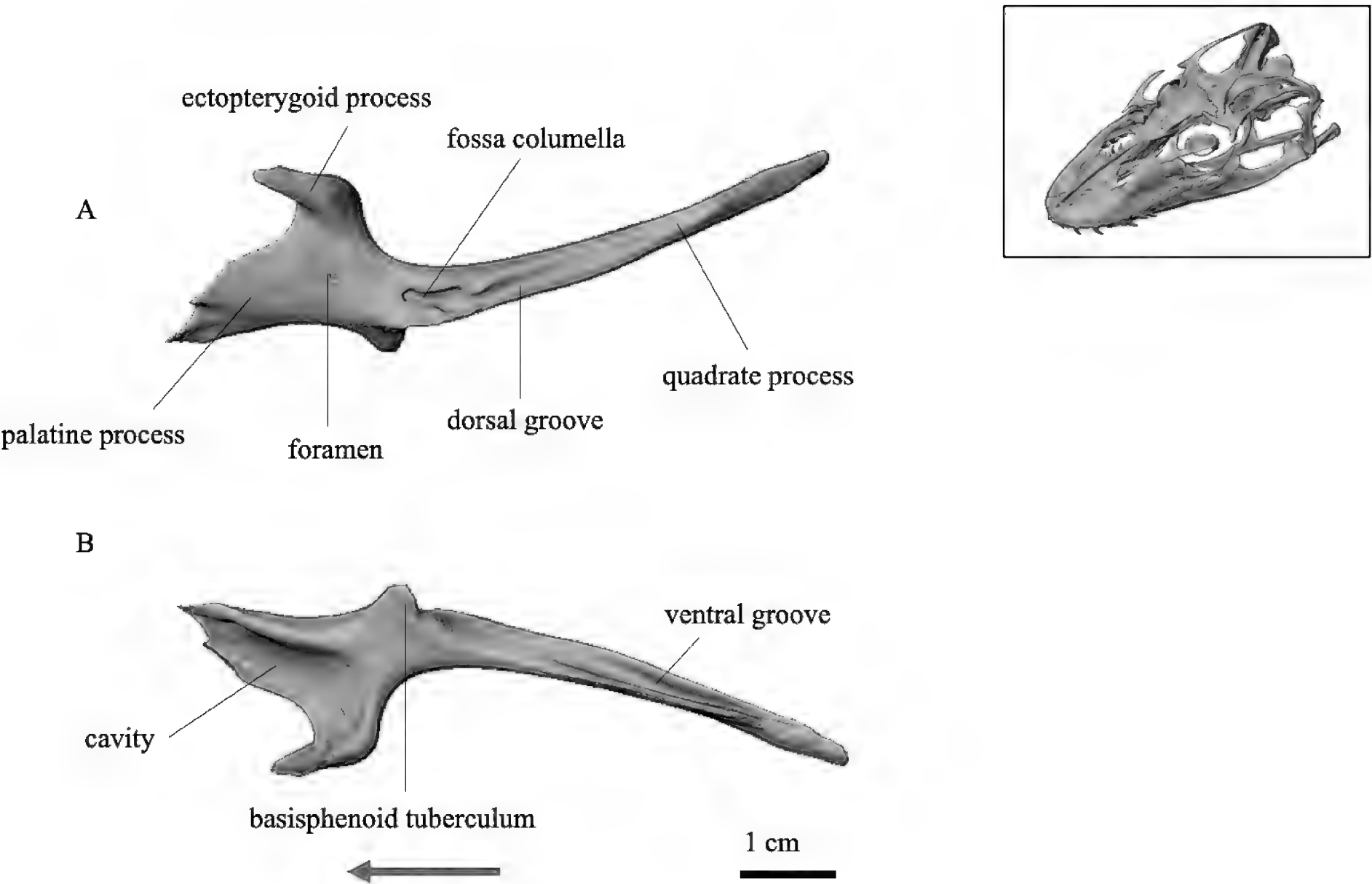
Figure 24. Pterygoid. **A.** Right pterygoid in dorsal; **B.** In ventral views. Arrow pointing anteriad. Scale bar: 1 cm.

The epipterygoid is a paired bone, vertically elongated and cylindrical (Fig. 25). Its ventral end curves anteriorly and is accommodated by the pit of the pterygoid quadrate process. The dorsal end of the epipterygoid lies laterally and loosely against the anterior superior process of the prootic.

Occipital region — Braincase

The supraoccipital is a flat bone that forms the roof of the posterior braincase (Fig. 26). It has sutures laterally with the prootics and posteriorly otooccipital. The anterior part of the supraoccipital rises sharply upward and features a small ascending process (Fig. 26C) in the middle of the anterior margin that projects into the fossa of the parietal. The posterior part of the supraoccipital contributes together with the otooccipital and basioccipital to the formation of the foramen magnum (Fig. 26A).

The prootic is a paired bone located on the dorsolateral side of the braincase (Fig. 26). It articulates anteriorly with the alary process of the basisphenoid, with the supraoccipital and the otooccipital laterally. The prootic also forms three processes: the dorsal, rounded anterior superior process (Fig. 26C), the ventral, shorter anterior inferior process (Fig. 26C), and the long posterior process (Fig. 26C). The anterior superior process rises sharply upward and is laterally flattened. It also establishes mobile connections with the parietal and epipterygoid, respectively.
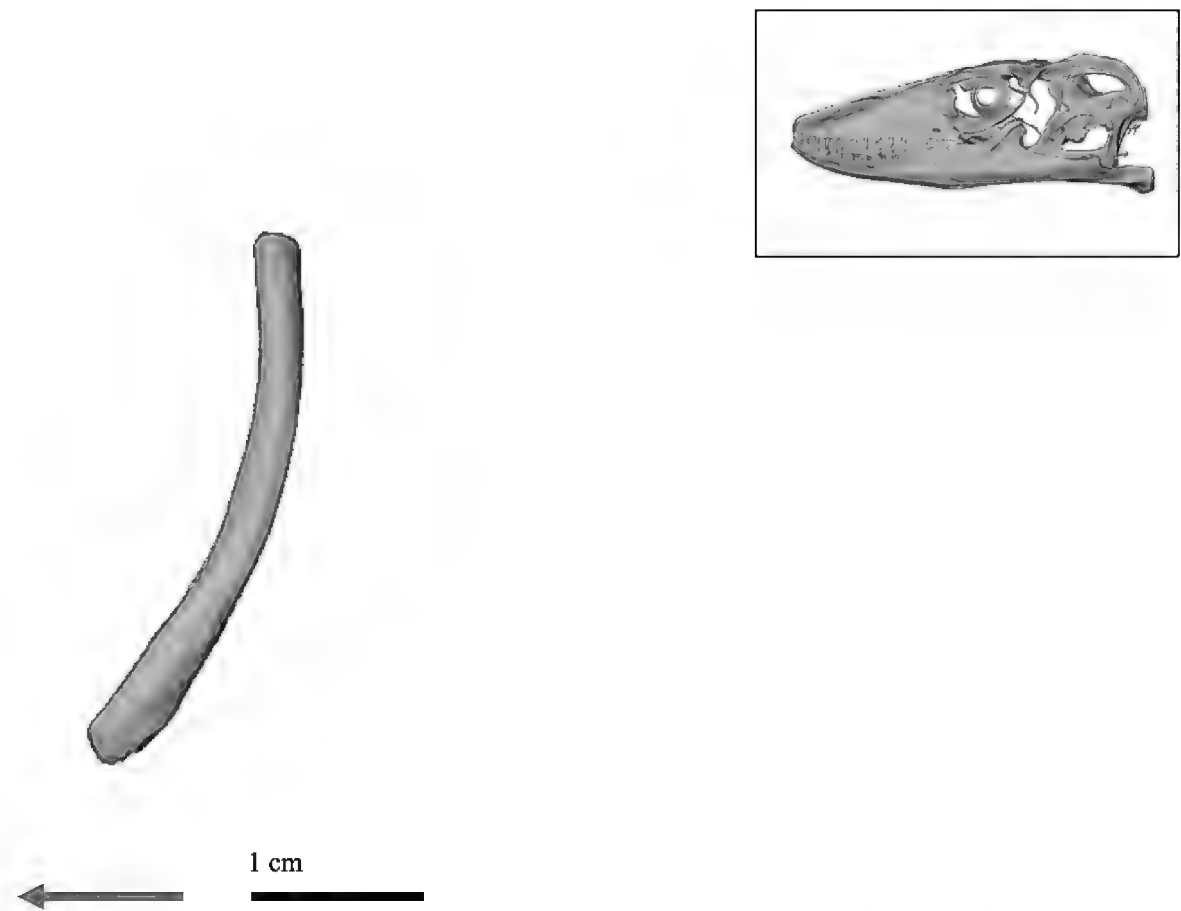
Figure 25. Left epipterygoid in lateral view. Arrow pointing anteriad. Scale bar: 1 cm.
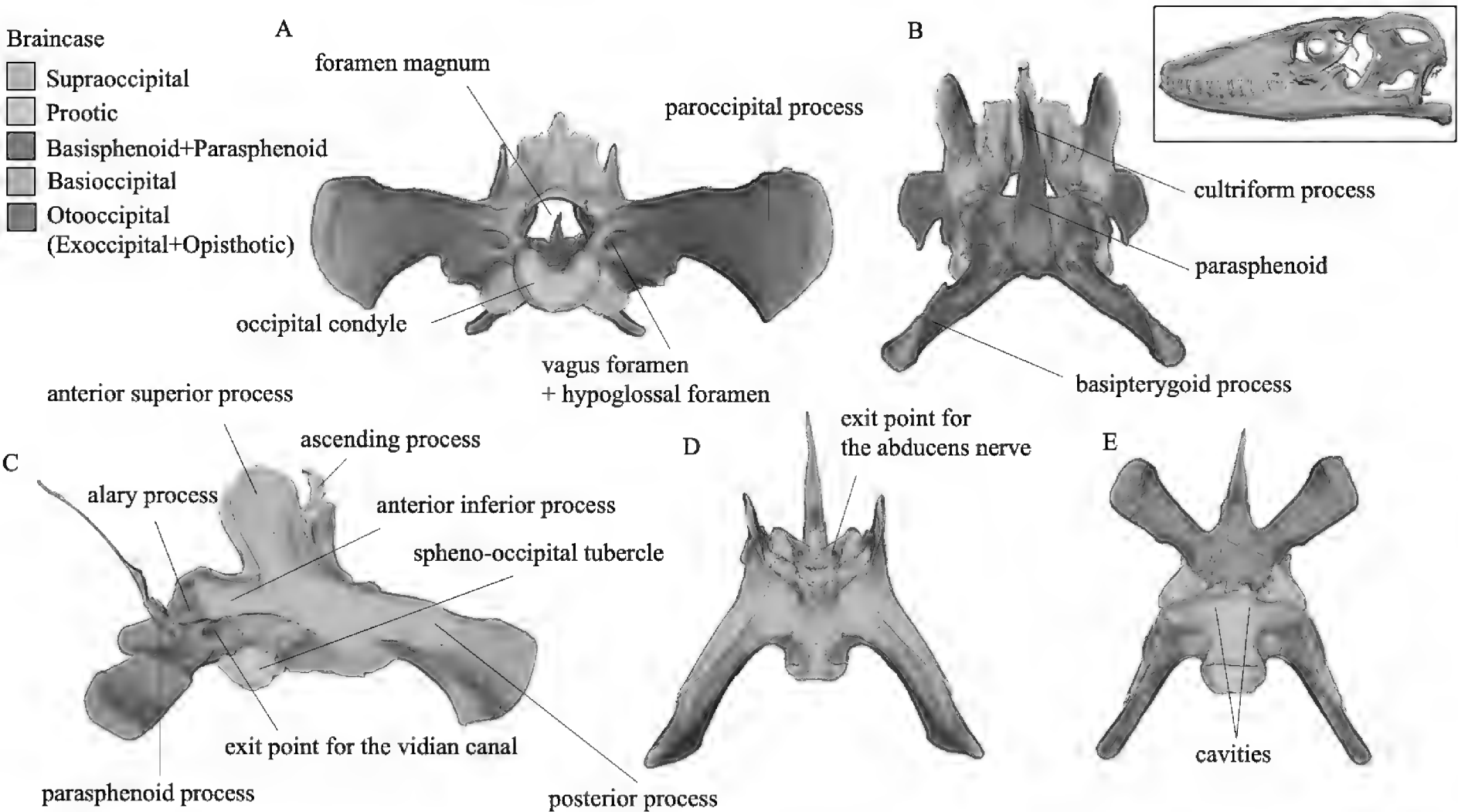
Figure 26. Braincase. **A.** In posterior; **B.** In anterior; **C.** In lateral; **D.** In dorsal; **E.** In ventral views.

The basisphenoid is an unpaired bone that forms the anterior floor of the braincase (Fig. 26). The parasphenoid (Fig. 26B), which is long and flattened, is fused to the basisphenoid and extends anteriorly from its front margin. The parasphenoid forms a cultriform process at its anterior end (Fig. 26B). The basisphenoid also features a small parasphenoid process (Fig. 26C) at the origin of the parasphenoid, bearing two adjacent depressions (Fig. 27B). The dorsal, smaller alary process (Fig. 26C) attaches to the anterior inferior process of the prootic. Posteriorly, the basisphenoid shares a suture with the otooccipital. The ventral, long, ventrolaterally projecting basipterygoid process (Fig. 26B) movably articulates with the pterygoid. At the starting point of the basipterygoid process, a pair of foramina serves as entry point for the vidian canal (Fig. 27B). Dorsal to this, on the alary process, is another pair of foramina through which the abducens nerve passes (Fig. 27B cf. Shrivastava 1964). Between the two foramina pairs lies the hypophyseal fossa (Fig. 27B), housing the paired internal carotid foramen (Fig. 27B) that is connected to the vidian canal.

The otooccipital is a paired bone and composed of the exoccipital and opisthotic. It contacts the supraoccipital anterodorsally, the prootic anterolaterally, the basisphenoid anteriorly and the basioccipital ventrally (Fig. 26). The otooccipital has a long, massive, laterally compressed paroccipital process (Fig. 26A) that projects posterolaterally. Its posterior end approaches the supratemporal laterally. An intercalar element is adjacent to the cephalic condyle of the quadrate (Fig. 17E). On either side of the foramen magnum, a relatively large opening is present, representing the fusion of the vagus foramen and hypoglossal foramen (Fig. 26A). At the junction of the primary exoccipital and opisthotic, the superior oval window and the inferior fenestra rotunda can be observed (Fig. 27A). At the junction with the prootic, two widely separated fa-cial foramina are present (Fig. 27A). The oval window accommodates the proximal end of the columella.

The basioccipital, an unpaired bone that forms the base of the posterior braincase (Fig. 26), contacts the basisphenoid anteriorly, the otooccipital dorsally. It consists of two major components: the anterior, lateral spheno-occipital tubercles (Fig. 26C) and the posterior, medial occipital condyle (Fig. 26A). The ventral side of the basioccipital is concave (Fig. 26E).
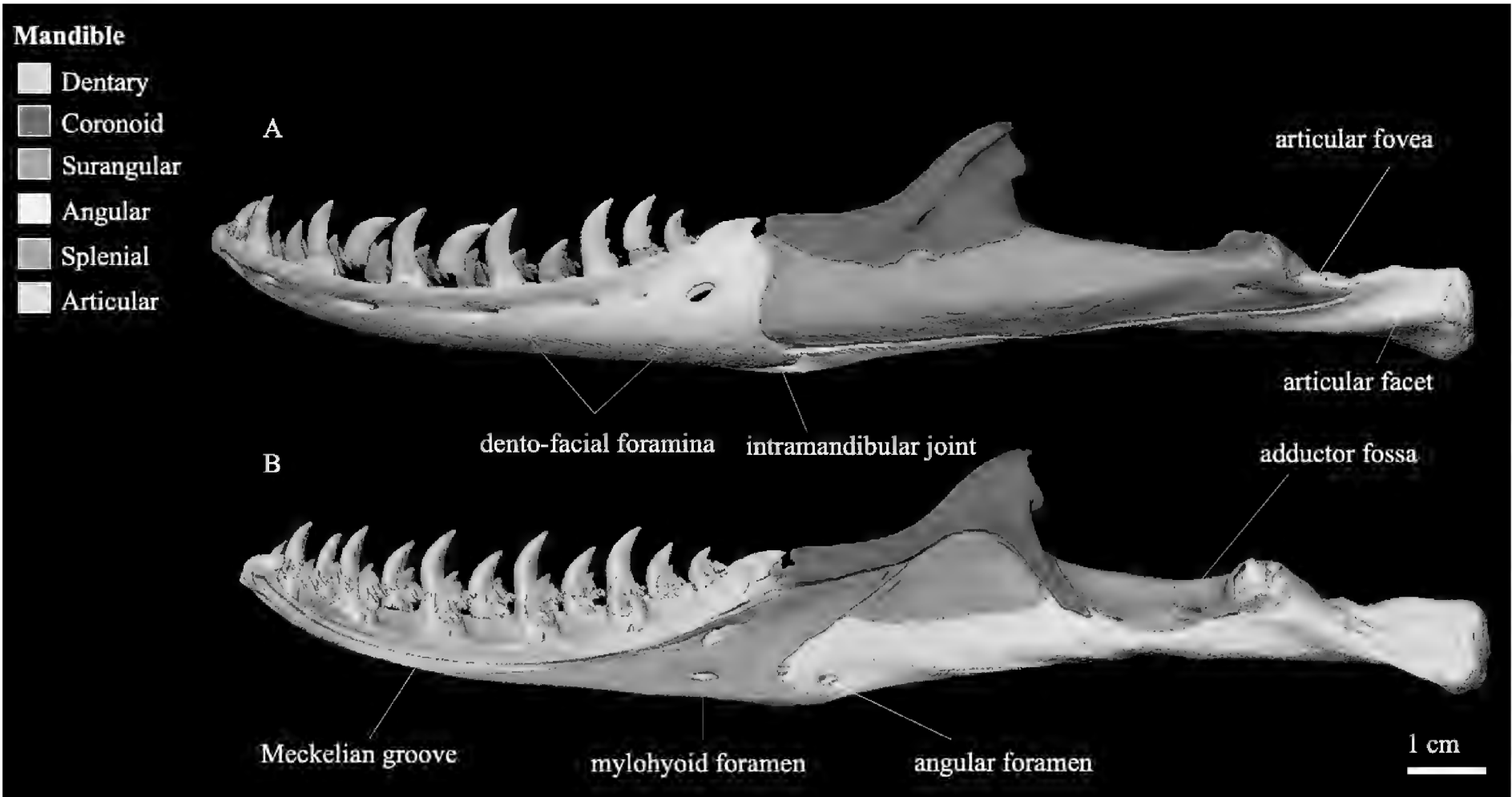
Mandible

The dentary constitutes the most anterior part of the mandible (Fig. 28). It articulates with the coronoid, surangular, and angular posteriorly. The long Meckelian groove is discernible on its medial side (Fig. 29B), but most of it is covered by the splenial. Towards the posterior end, the dentary has two small processes: the dorsally positioned coronoid process and the ventrally located angular process (Fig. 29A). Along the upper lateral face of the dentary, a series of dentofacial foramina is present (Fig. 29A). The posteriormost foramen has a significantly larger opening than the anterior foramina. Each of the two dentaries bears twelve teeth. The teeth are sharp, laterally compressed, and posteriorly curved. The dentary also accommodates three to four smaller replacement teeth for each working tooth, each located directly medial to the respective working tooth.

The coronoid of the mandible is a laterally flattened bone that has three processes (Fig. 30). The long and thin anterior process (Fig. 30A) has a bifurcation; its outer side articulates with the dentary, and its inner side with the splenial. The dorsal masseteric process (Fig. 30A) is broad, rising steeply dorsally, and curving slightly medially, with a thickened upper margin on both inner and outer sides.
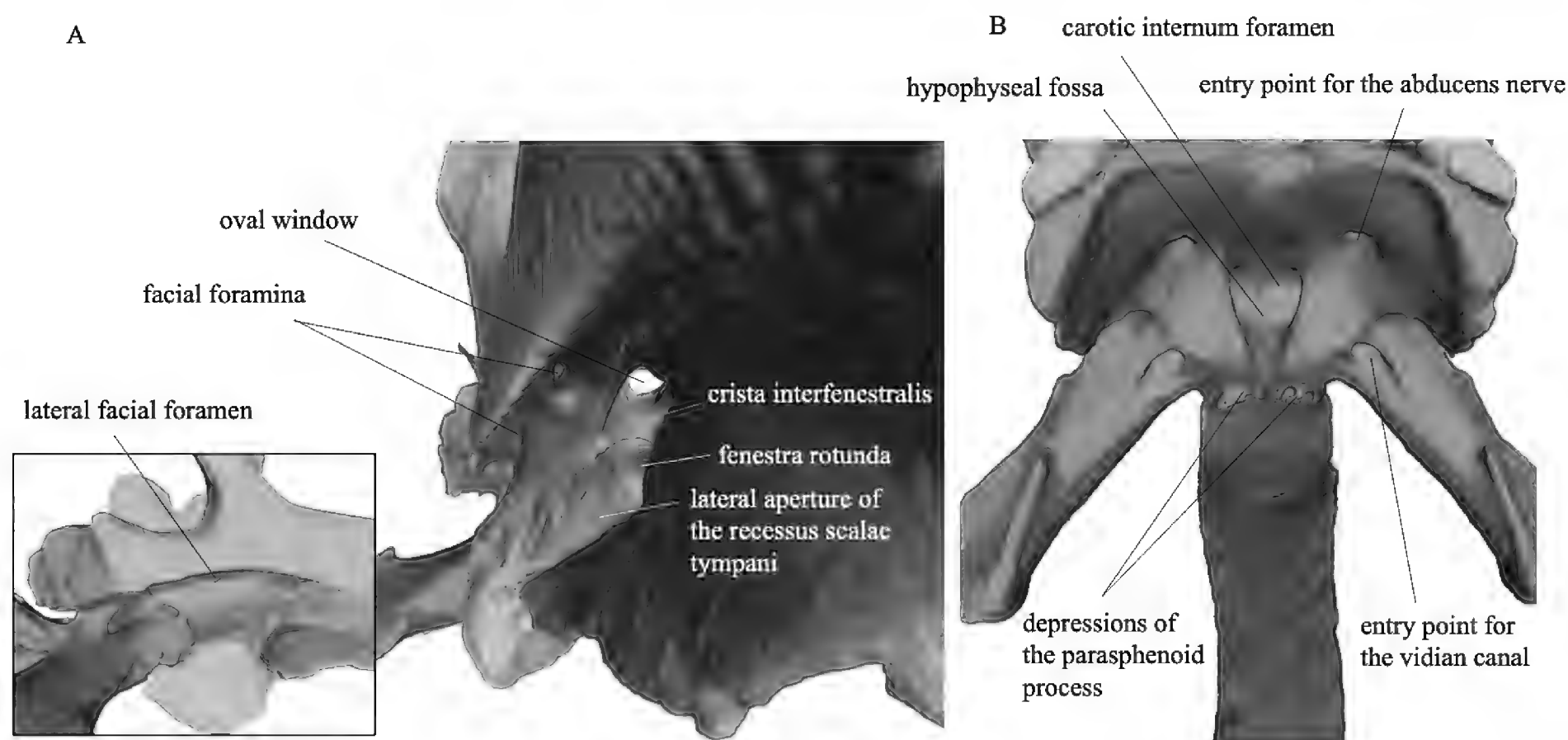
Figure 27. Braincase. **A.** In posterolateral view. Crista interfenestralis divides the oval window and the lateral aperture of the recessus scalae tympani. The lateral aperture of the recessus scalae tympani has an elongated, slit-like shape. The facial foramina are widely separated; **B.** The basisphenoid and parasphenoid in anterodorsal view.

Figure 28. Mandible of *Varanus komodoensis* (ZMH R13322). **A.** Left mandible in lateral view; **B.** Right mandible in medial view. Scale bar: 1 cm.
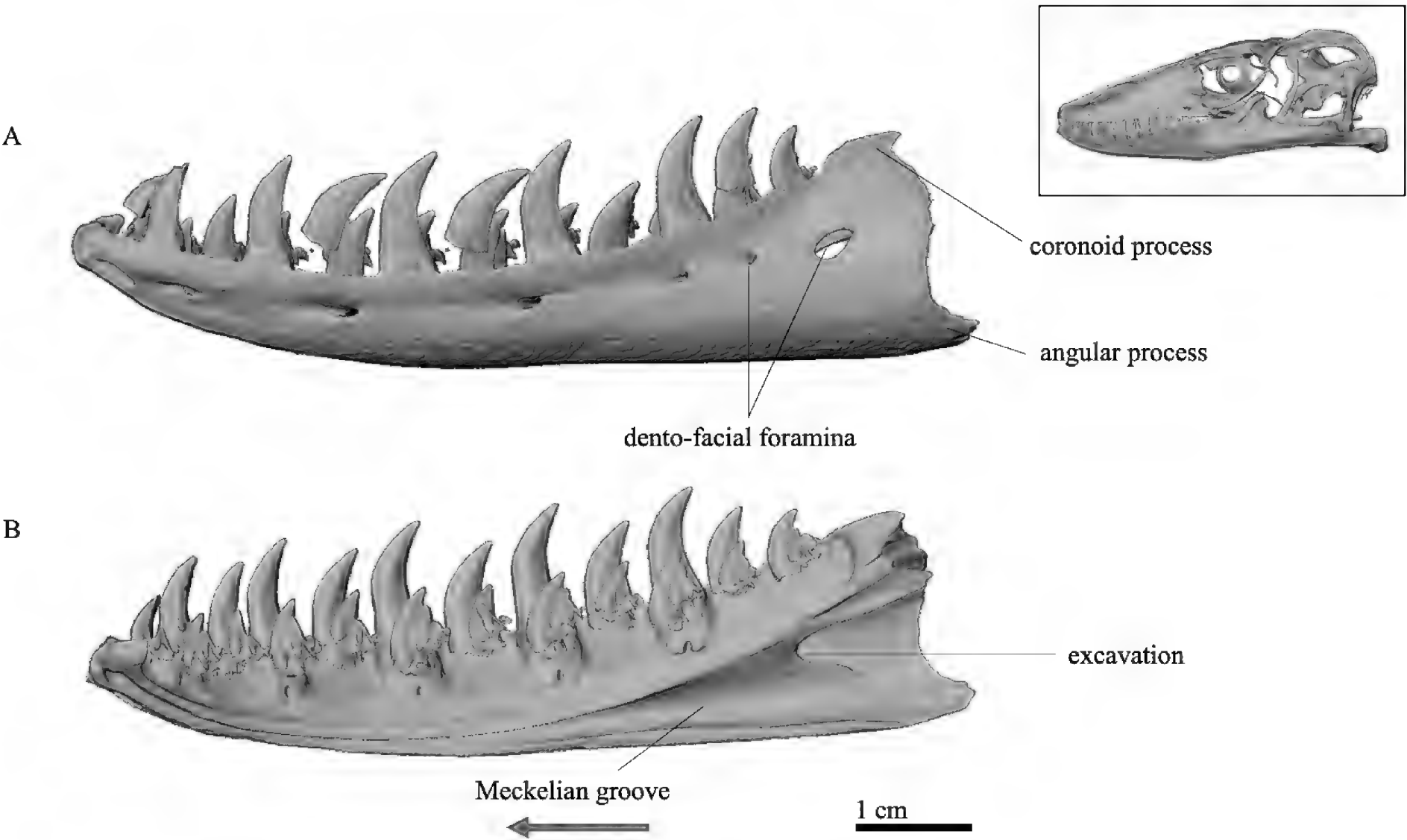
Figure 29. Dentary. **A.** Left dentary in lateral view; **B.** Right dentary in medial view. Arrow pointing anteriad. Scale bar: 1 cm.

The ventral posterior process of the coronoid (Fig. 30A) extends strongly ventrally and reaches the articular. The ventral margin of the coronoid is laterally flattened and is placed on top of the surangular.

The surangular constitutes approximately half of the mandible length (Fig. 31). It establishes contact anteriorly with the dentary and splenial. The coronoid process of the surangular, located laterally (Fig. 31A), articulates with the dorsally attached coronoid. There is also an anterior surangular foramen beneath this process. This looks like a pit on the image, but it should be due to a CT artifact (Fig. 31A). Ventrally, the surangular is tightly interlocked with the angular. The medial surface of the surangular forms a long suture with the articular. Most of the lateral surface of the articular is covered by the surangular. The lateral surface of the surangular is convex, and a foramen is present at the posterior end (Fig. 31A), two additional pits are present on the medial side of the bone posteriorly

(Fig. 31B). The posterior end of the surangular has a cavity that takes up a part of the articular (Fig. 31B). Both the surangular and the articular contribute in the formation of the adductor fossa (Fig. 31C), which opens as a medial gap in the suture between the two bones.

The angular is a slender and small bone (Fig. 32), forming a long lateral suture with the articular and articulating anteriorly with the dentary. A long ridge on the outer side of the angular contacts the surangular. The medial side of the angular is flat and exhibits the angular foramen (Fig. 32B).
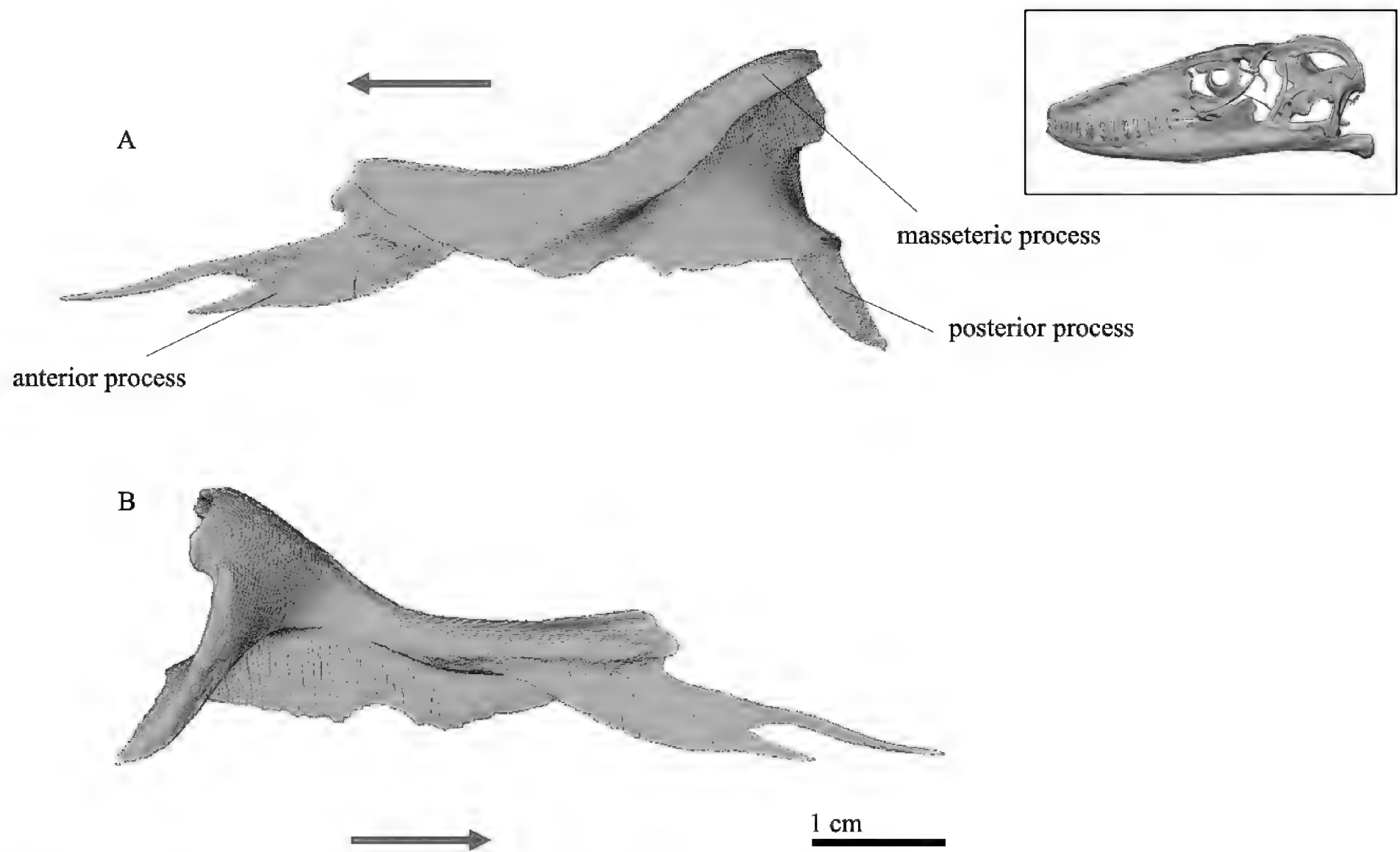
Figure 30. Coronoid. **A.** Left coronoid in lateral; **B.** In medial views. Arrows pointing anteriad. Scale bar: 1 cm.
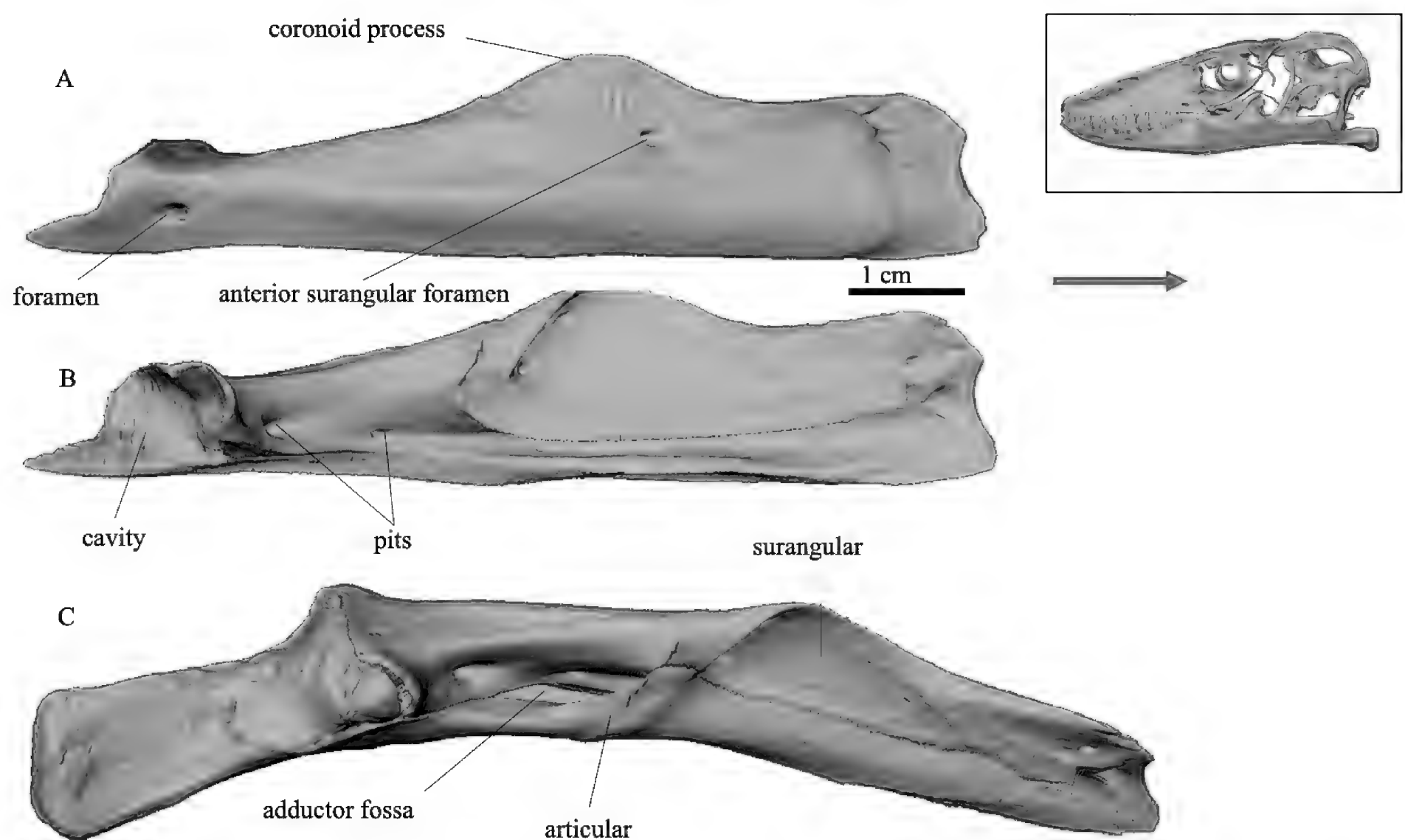
Figure 31. Surangular. **A.** Right surangular in lateral view; **B.** Left surangular in medial view; **C.** Adductor fossa in the context of surangular and articular bones, dorsolateral view. Arrow pointing anteriad. Scale bar: 1 cm (**A, B**).
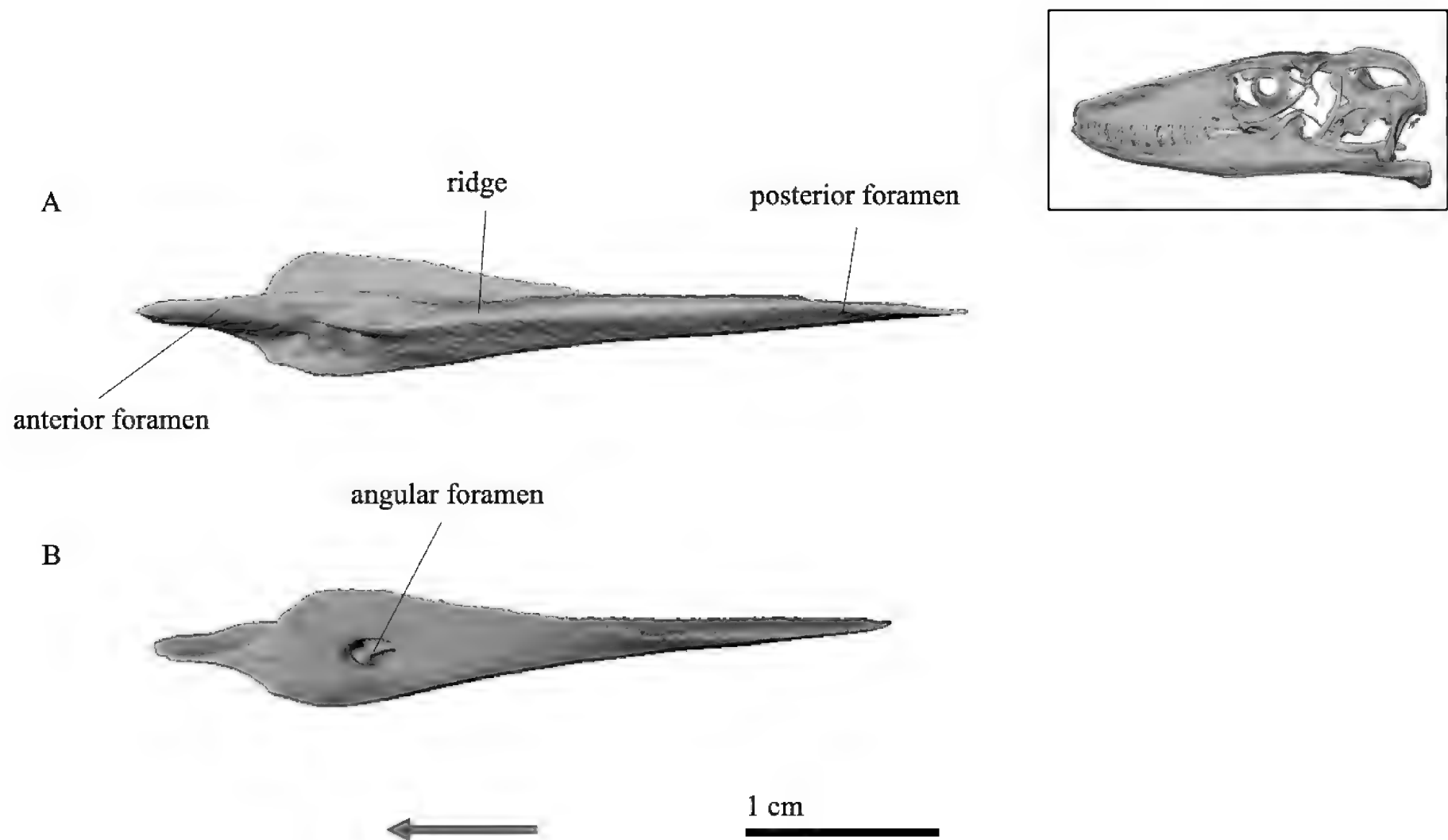
Figure 32. Angular. **A.** Left angular in lateral view; **B.** Right angular in medial view. Arrow pointing anteriad. Scale bar: 1 cm.

The splenial, a flat bone located on the medial side of the mandible (Fig. 33), features three major pointed processes (Fig. 33A). The anterior process forms a long suture with the dentary. The broad, blade-like posterodorsal process attaches laterally to the coronoid and articulates posteriorly with the surangular and articular. The posteroventral process (Fig. 33A) contacts the angular. The medial side of the splenial is smooth, while the outer side has a horizontal ridge on which the mylohyoid foramen is located (Fig. 33A).

The articular is an elongated bone that comprises the posteriormost part of the mandible (Fig. 34). The anterior part of its lateral side is covered by the surangular. The anterior prearticular process (Fig. 34A) attaches to the splenial and angular. The posterior part of the prearticular process rises upward and contacts with the coronoid. Behind this eleva-

Figure 33. Splenial. **A.** Left splenial in lateral view; **B.** Right splenial in medial view. Arrow pointing anteriad. Scale bar: 1 cm.
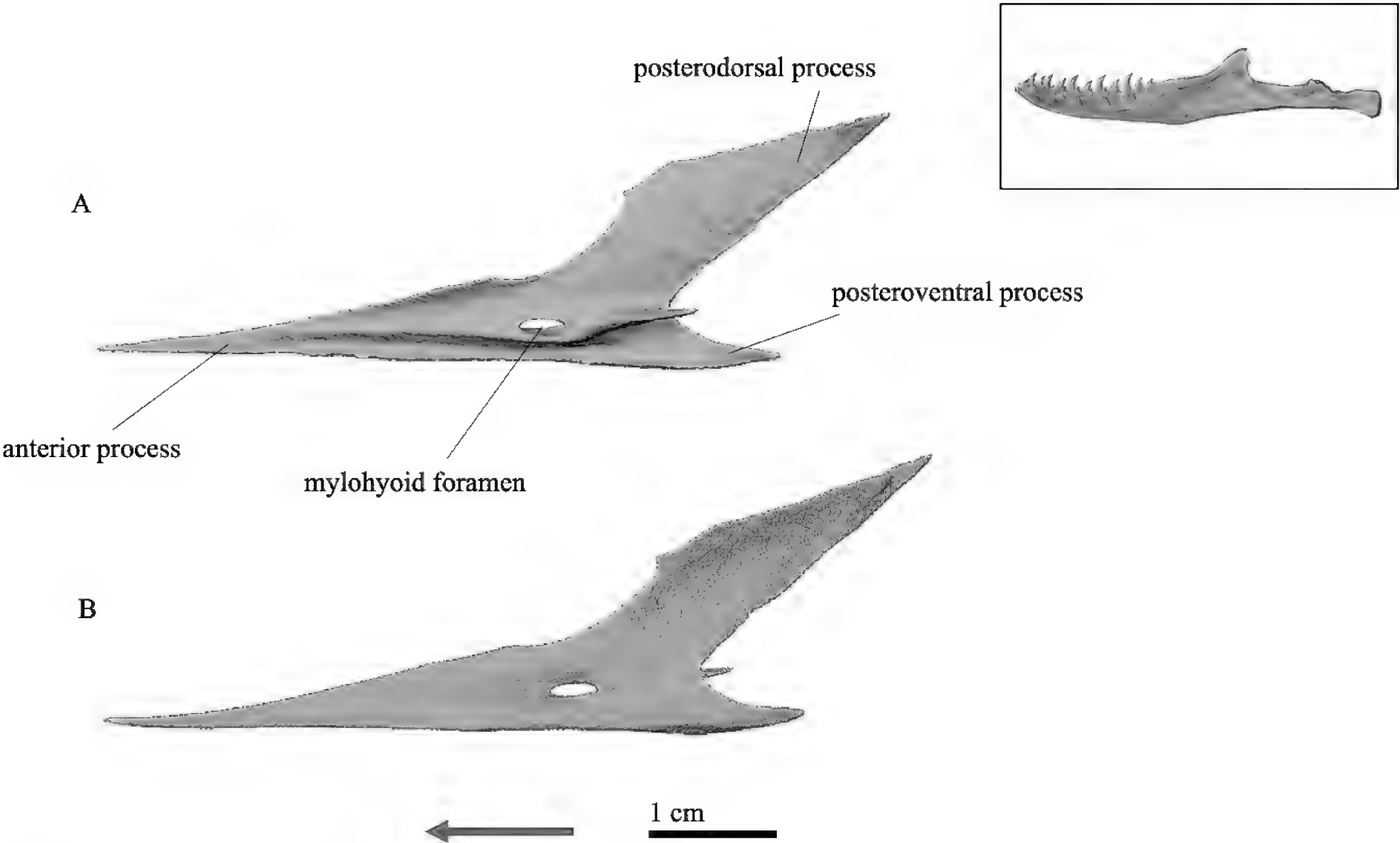
Figure 34. Articular. **A.** Left articular in lateral view; **B.** Right articular in medial view. Arrow pointing anteriad. Scale bar: 1 cm.
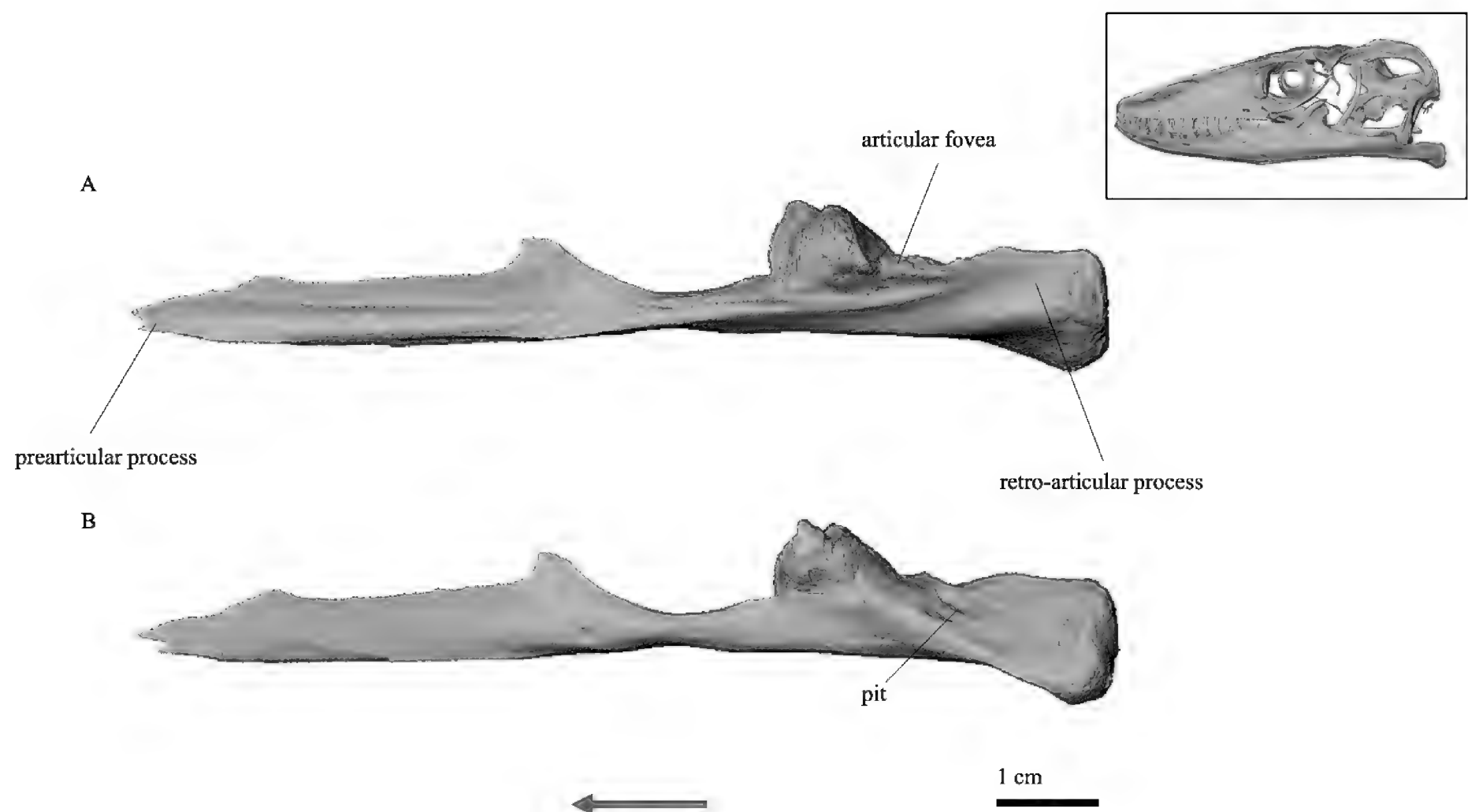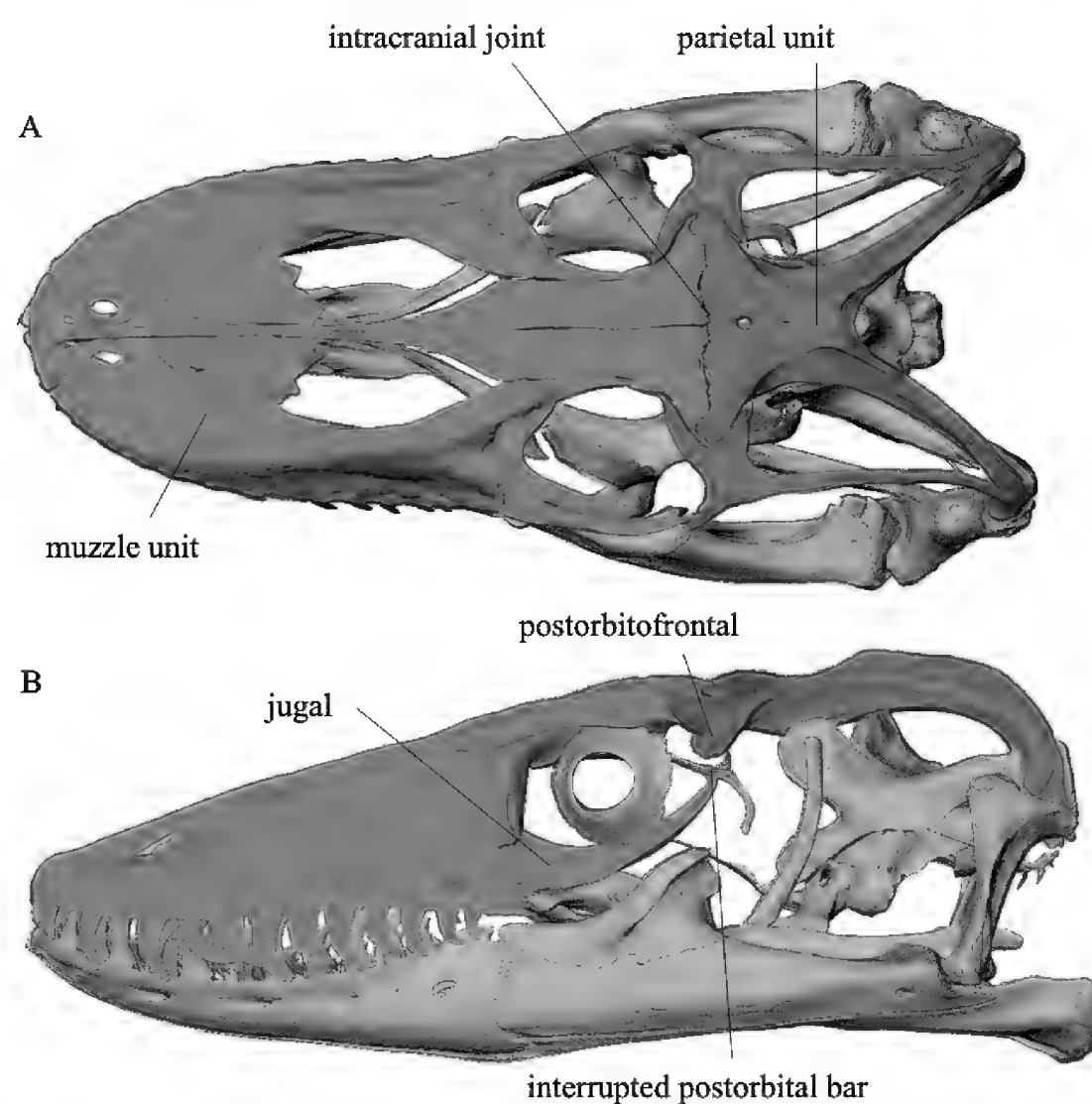

Figure 35. Skull of *Varanus komodoensis* (ZMH R13322). Muzzle unit (premaxilla, maxilla, septomaxilla, nasal, prefrontal, frontal, supraorbital, lacrimal, and jugal) in red, parietal unit (parietal, squamosal, supratemporal, postorbitofrontal) in blue. **A.** In dorsal view. Between the frontal and parietal is the intracranial joint; **B.** In lateral view. The jugal and postorbitofrontal are not in contact.

tion, the articular narrows, and directly behind the narrowing is a round outgrowth. Behind the outgrowth, the articular fovea opens (Fig. 34A), receiving the mandibular condyle of the quadrate. A pit is present just posterior to the articular fovea (Fig. 34B). While the anterior prearticular process is laterally flattened, the posterior retro-articular process (Fig. 34A) thickens, forming the free end of the mandible.

Discussion

Cranial kinesis

In the 3D reconstruction of the *Varanus komodoensis* skull, a postorbital bar is present. However, the orbital process of the postorbitofrontal is not connected to the temporal

process of the jugal (see Fig. 35B). Additionally, the muzzle unit and the parietal unit exhibit a loose connection in the parietal region (see Fig. 35A). Notably, an intracranial joint between the parietal and frontal is observed, a characteristic feature of skull mesokinesis (Frazzetta 1962, 1986). Metzger (2002) previously noted that taxa exhibiting mesokinesis typically either lost or significantly reduced the postorbital bar. The skull of *V. komodoensis* is an example of this general rule, as clearly demonstrated in the digital dissection of the examined specimen.

This observation suggests a functional interdependence between the reduction or absence of the postorbital bar and the acquisition of mesokinesis. The details of the *Varanus komodoensis* skull anatomy underscore the significance of this interdependence, stimulating further functional hypotheses on the structural adaptations associated with mesokinetic features.

The lower temporal bar is absent in the *Varanus komodoensis* skull as generally in squamates. This reduction is linked to the evolution of streptostyly, a phenomenon enabling the quadrate to freely oscillate in both anterior and posterior directions (Starck 1979). An alternative hypothesis (Metzger 2002) suggests that the primary purpose of reducing the lower temporal bar is to accommodate larger lateral adductor musculature. While the precise selective pressures driving this evolutionary change remain unclear, both streptostyly and the increase in relative size of jaw musculature most likely have adaptive advantages in predatory varanids.

The skull of monitor lizards manifests several movable articulations between distinct bone segments. Bahl (1937) delineated the locations of these mobile connections in monitor lizards: between the supraoccipital and parietal, between the anterior superior process of the prootic, between the parietal, the basipterygoid process of the basiphenoid and the pterygoid, and between the paroccipital process of the otooccipital and the quadrate and supratemporal. Mertens (1942b) identified a loose connection between the prefrontal and palatine, interrupted by gaps. It is noteworthy, that skull kinesis and mobility exhibit age-dependency, potentially less pronounced in older individuals compared to their younger counterparts (Starck 1979). If this applies to the *V. komodoensis* remains to be shown.

Cranial morphology

The skull of *Varanus komodoensis* exhibits a highly fenestrated structure, a theme shared with many extant and extinct diapsids, such as lizards, tuatara, dinosaurs, and crocodiles. The shapes of these skulls are strongly associated with feeding behavior (Curtis et al. 2011). Moreno et al. (2008) reported that the "space-frame" skull morphology of *V. komodoensis* differs significantly from that of most large prey specialists. This "space-frame" skull design is considered to be optimized for the distinctive hold-and-pull feeding technique employed by *V. komodoensis*, reflecting its biology as an active predator (D'Amore et al. 2011). From a functional morphological perspective,

kinetic movements within the skull of *Allosaurus fragilis* and *Varanus komodoensis* have been referred to as comparable (Rayfield et al. 2001). In that study on the heavily fenestrated skull of the therapsid *A. fragilis*, Rayfield et al. (2001) identified functional loops that route compressive vectors caused by biting around large cranial fenestrae. These loops serve to minimize stress and strain in response to applied forces. Building upon this, it is conceivable that the "space-frame" cranial morphology of *V. komodoensis* also plays a pivotal role in stress management during biting. Such observations can only suggest possible similar diets and feeding biomechanics but have no phylogenetic significance.

Teeth, being the first structures involved in food contact and processing, generally exhibit morphologies closely correlated with a species' dietary habits (Lönnberg 1928; Rieppel 1979). The teeth of *Varanus komodoensis* are classified as ziphodont, featuring laterally flattened, posteriorly curved, and serrated characteristics. Additionally, they are polyphodont, with teeth alternating continuously in succession. Simultaneously, they are conspicuously pleurodont, as the base of the teeth unilaterally fuses to the elevated inner margin of the jawbone (Fig. 5C; Auffenberg 1981). While the serrated margin of the posterior tooth edges was not visible in the visual representation of the examined specimen (see Fry et al. 2009; Janeczek et al. 2023), we attribute this to potential limitations in the CT scanning resolution.

The specimen examined displayed eight teeth on the premaxilla (Fig. 4B), 13 teeth on the maxilla (Fig. 5B), and twelve teeth on the dentary (Fig. 29). The numbers in the maxilla and dentary align with descriptions by Lönnberg (1928), Mertens (1942b), and Auffenberg (1981). However, the latter two authors noted a discrepancy in the premaxilla, with *Varanus komodoensis* having seven teeth, while Lönnberg reported only six premaxillary teeth. This disparity suggests potential intraspecific variability in premaxillary dentition.

Varanus komodoensis employs a distinct pulling technique in both the hunting, defleshing, and dismembering of prey (D'Amore and Blumensehine 2009; D'Amore et al. 2011). This behavior matches well with the specific tooth morphology. While monitor lizards typically consume prey smaller than themselves, adult *V. komodoensis* primarily target large to exceptionally large mammals (Bennett 1996). Successful predation on larger prey necessitates an efficient killing technique and corresponding dental adaptations. D'Amore et al. (2011) proposed that the ziphodont teeth of *V. komodoensis*, coupled with caudal head movements, facilitate direct contact between the curved tips of the teeth and the flesh. Consequently, the laterally flattened and posteriorly serrated teeth can traverse through the flesh with minimal resistance. This mechanism effectively inflicts deep wounds in the hunted prey and tears the flesh into manageable pieces of the carcass, subsequently facilitating ingestion. *Varanus komodoensis* employs not only its sharp, serrated teeth but also coagulopathic, hypotensive, hemorrhagic, and shock-in-

ducing toxins during prey capture (Fry et al. 2009). The venom glands of *V. komodoensis*, positioned between ziphodont, pleurodont teeth. The teeth themselves lack grooves typically associated with venom delivery in helodermatid lizards or viperid snakes (Fry et al. 2009).

Intriguingly, D'Amore et al. (2011) reported that *V. komodoensis* exhibits a significantly lower bite force compared to other vertebrates of similar body mass. However, this seemingly weak jaw adduction force is complemented by a strong pulling force in the ventrocaudal direction, exerting a considerably greater force than the bite itself. Moreno et al. (2008) asserted that the skull of *V. komodoensis* is highly optimized to concurrently execute a jaw adductor-driven bite and a postcranially generated pull-back, distinguishing it from a jaw-driven only bite. Consequently, pulling plays a pivotal role in both the predation and feeding processes. This perspective is supported by a study demonstrating that the Komodo dragon skull is specifically adapted to endure the forces generated during pulling (Fry et al. 2009).

It has been proposed that *Allosaurus fragilis* and other theropods, which exhibits a "spaceframe" skull design and ziphodont tooth morphology reminiscent of *V. komodoensis*, may have employed a comparable killing strategy (Rayfield et al. 2001; Rayfield 2005; Snively et al. 2013). The finite element analysis (FEA) of the *Allosaurus* skull in their study indicated a weak bite force relative to its body mass, similar to *V. komodoensis*. These shared features in distantly related predators may suggest convergent evolution of biomechanical adaptations for a specific predatory behavior.

Varanoid species that feed on large prey relative to their body size exhibit elongated skulls and mandibles (McCurry et al. 2015). This also holds true for *Varanus komodoensis*. The elongated lower jaws in this species have been suggested to enhance the tearing of prey flesh during the pull-back motion (McCurry et al. 2015). Additionally, a longer mandible could accommodate more teeth, potentially increasing the efficiency of prey processing. Furthermore, elongated skulls may facilitate better access to certain parts of a carcass (McCurry et al. 2015).

Osteoderms occur in most tetrapods and hold significant importance within squamates from a phylogenetic perspective (e.g., Maisano et al. 2019; Kirby et al. 2020; Williams et al. 2021). Morphological characteristics such as structure (single vs. compound), interrelation (imbricate vs. abutting vs. isolated), distribution (presence vs. absence, cephalic vs. body, dorsal vs. ventral), and ornamentation (smooth vs. rugose) have been utilized as morphological character states (Maisano et al. 2019). However, in taxa where osteoderm platelets are small and isolated within the skin, dissection yields limited insight into their spatial arrangement in life (Maisano et al. 2019). Utilizing sufficiently resolved CT scanning, the original pattern and position of the *Varanus komodoensis* osteoderm could be visualized (Maisano et al. 2019; this study). Four basic forms—rosette, platy, dendritic, and vermiform—classify the individual osteoderm elements of *V. komodoensis* (Maisano et al. 2019). The lateral side of the skull exhibits an exceptionally fine

and dense structure with dendritic platelets (visible in Maisano et al. 2019, fig. 1) that we could not fully segment in our dataset due to time restrictions (Fig. 3C).

In the *Varanus komodoensis* specimen examined, the osteoderm is either reduced or absent in several areas, parietal region, frontoparietal suture, parietal foramen, snout, along the lip margins, and at the ears. Cephalic osteoderms have been hypothesized to contribute to the prevention of mesokinetic movements in some lizards (Barahona and Barbadillo 1998). The reduction or absence of osteoderm at mobile joints and sensory organs in *V. komodoensis* suggests a potential interference of osteoderm with the movement of kinetic regions and the reception of environmental stimuli (Maisano et al. 2002). The absence of osteoderm at the frontoparietal suture, functioning as an intracranial joint in mesokinesis, may be considered a morphological correlate of skull mesokinesis. This reduction or absence of osteoderm in specific areas has also observed in *Lanthanotus borneensis* Steindachner, 1878, the closest relative of varanids (Maisano et al. 2002). Ontogenetic differences in the presence of cephalic osteoderms of other lizards, were described, for example, by Bever et al. (2005), and may occur in *V. komodoensis*.

Cranial features and phylogenetic relationship of the monitor lizards

The family Varanidae encompasses the extant genus *Varanus* and approximately nine extinct genera, with the earliest known from the late Cretaceous period (Dong et al. 2022). Presently, the genus *Varanus* comprises 86 recognized extant species (Uetz et al. 2023). Morphological and/or molecular data have led to the subdivision of the genus into eleven subgenera. *Varanus komodoensis* belongs to the subgenus *Varanus*, which encompasses a total of eight species (Auliya and Koch 2020).

The closest relative of Varanidae is the family Lanthanotidae. The Varanidae+Lanthanotidae clade represents the sister group of Shinisauridae and is placed within Anguimorpha. The Anguimorpha, together with Iguania and Serpentes, collectively constitute the Toxicofera group within Squamata (Pyron et al. 2013).

To investigate the phylogeny of squamates, Gauthier et al. (2012) assembled a dataset of 192 species (51 extinct and 141 extant) and 976 apomorphies distributed among 610 phenotypic characters. Within this dataset, 26 characters were identified as synapomorphies for *Saniwa+Varanus*, with 11 specifically related to cranial morphology:

1. Premaxilla internasal process (nasal process) length: more than half way to frontal between nasals (Fig. 1A).
2. Premaxilla internasal process (nasal process) shape in cross-section: compressed (Fig. 4C).
3. Frontal subolfactory processes (lateroventral process): arch beneath brain to articulate on ventral midline (Fig. 8C).

4. Postorbital jugal ramus (orbital process): level with quadrate head.
5. Lacrimal foramen number: divided through to olfactory surface (Fig. 11E).
6. Jugal postorbital ramus development: incomplete bony postorbital bar (Fig. 2A).
7. Vomer ventral longitudinal ridges: discrete parasagittal canals anteriorly on vomer delimited by lateral and median ridges (Fig. 21B).
8. Palatine teeth: absent (Fig. 22).
9. Pterygoid teeth: absent (Fig. 24).
10. Epipterygoid-parietal contact: absent (Fig. 2).
11. Cultriform process: long (Fig. 26B).

All characters were validated in the skull of *Varanus komodoensis*. Comparison with macerated skulls of four distinct varanid species (*V. albigularis* Daudin, 1802 ZMH R06503, *V. exanthematicus* Bosc, 1792 ZMH R12221, *V. niloticus* Linnaeus, 1766 ZMH R06504, *V. griseus* Daudin, 1803 ZMH R14035) further confirmed the synpomorphies of *Varanus* species.

Regarding the taxonomic affiliations of *Varanus komodoensis*, Head et al. (2009) proposed a close relationship between *V. komodoensis* and the extinct *V. priscus* (*Megalania*) based on the osteological characters of the neurocranium. Six characters within the braincase were identified as unequivocal synapomorphies, two as variable characters shared between these two species:

1. Crista prootica posterior process: reduced (0); tall tabular, or curved rhomboidal process (1). In *V. priscus*, the character state was 0. In the Komodo dragon, the character is polymorphic state 0 or 1. In our specimen: 1; tall tabular (Fig. 26C).
2. Oval window and occipital recess: narrowly separated, overlapped by crista interfenestralis in lateral view (Fig. 27A).
3. Oval window: dorsal or posterior to spheno-occipital tubercle (Fig. 27A).
4. Occipital recess: slit (Fig. 27A).
5. Facial foramen: not divided (0); short or incomplete separation (1); wide separation, separation fully ossified (2). *V. priscus* has the character state 2. In the Komodo dragon, this character varies between character state 1 and 2. In this specimen: 2; separated wide (Fig. 27A, B).
6. Median ridge on supraoccipital: present, tall (Fig. 26).
7. Supraoccipital dorsal process: narrow, defined by deep lateral recesses (Fig. 26C).
8. Supraoccipital ascending process: ossified (Fig. 26C).

Fry et al. (2009) postulated, based on morphological characteristics of the skull, that *Varanus priscus* employed a combination of ziphodont teeth along with coagulopathic and hypotensive venom in its hunting strategy, analogous to the Komodo dragon.

Acknowledgements

References

Auffenberg W (1981) The behavioral ecology of the Komodo monitor. University Press of Florida, Gainesville, 406 pp.

Auliya M, Koch A (2020) Visuelle Bestimmungshilfe für die Waranarten der Welt (Gattung *Varanus*). Anleitung zur Identifikation von Waranen mit aktuellen Verbreitungsangaben sowie Kurzerläuterungen zu Reproduktionseigenschaften und Zucht in Haltung als Hilfestellung für Behörden des Artenschutzvollzugs. Bundesamt für Naturschutz, Bonn, 201 pp.

Bahl KN (1937) Skull of *Varanus monitor* (Linn.). Records of the Indian Museum 39: 133–174. https://doi.org/10.26515/rzsi/v39/i2/1937/162297

Barahona F, Barbadillo LJ (1998) Inter- and intraspecific variation in the post-natal skull of some lacertid lizards. Journal of Zoology 245(4): 393–405. https://doi.org/10.1111/j.1469-7998.1998.tb00114.x

Bellairs AD (1949) Observations on the snout of *Varanus*, and a comparison with that of other lizards and snakes. Journal of Anatomy 83(2): 116–146.

Bennett D (1996) Warane der Welt, Welt der Warane. Edition Chimaira, Frankfurt am Main, 383 pp.

Bever GS, Bell C, Maisano J (2005) The ossified braincase and cephalic osteoderms of *Shinisaurus crocodilurus* (Squamata , Shinisauridae). Palaeontologia Electronica 8: 1–36.

Bosc L (1792) *Lacerta exanthematica*. In: Société d'histoire naturelle de Paris (Ed.) Actes de la société d'histoire naturelle de Paris: Tome premier, premiere partie. L'Impr. de la Société, Paris, 25 pp.

Broeckhoven C, Du Plessis A (2018) X-ray microtomography in herpetological research: a review. Amphibia-Reptilia 39(4): 377–401. https://doi.org/10.1163/15685381-20181102

Curtis N, Jones MEH, Shi J, O'Higgins P, Evans SE, Fagan MJ (2011) Functional relationship between skull form and feeding mechanics in *Sphenodon*, and implications for diapsid dkull development. PLoS ONE 6(12): e29804. https://doi.org/10.1371/journal.pone.0029804

D'Amore DC, Blumensehine RJ (2009) Komodo monitor (*Varanus komodoensis*) feeding behavior and dental function reflected through tooth marks on bone surfaces, and the application to ziphodont paleobiology. Paleobiology 35(4): 525–552. https://doi.org/10.1666/0094-8373-35.4.525

D'Amore DC, Moreno K, Mchenry CR, Wroe S (2011) The Effects of biting and pulling on the Forces generated during feeding in the Ko-

modo Dragon (*Varanus komodoensis*). PLoS ONE 6(10): e26226. https://doi.org/10.1371/journal.pone.0026226

Daudin FM, Buffon GLL, Sonnini CS (1801) Histoire naturelle, générale et particulière des reptiles: ouvrage faisant suit à l'Histoire naturelle générale et particulière, composée par Leclerc de Buffon, et rédigée par C.S. Sonnini. 2. De l'imprimerie de F. Dufart, Paris, 432 pp. https://doi.org/10.5962/bhl.title.60678

Daudin FM, Buffon GLL, Sonnini CS (1802) Histoire naturelle, générale et particulière des reptiles: ouvrage faisant suite à l'Histoire naturelle générale et particulière, composée par Leclerc de Buffon, et rédigée par C. S. Sonnini. 3. De l'imprimerie de F. Dufart, Paris, 452 pp. https://doi.org/10.5962/bhl.title.60678

Daudin FM, Buffon GLL, Sonnini CS (1803) Histoire naturelle, générale et particulière des reptiles: ouvrage faisant suite aux oeuvres de Leclerc de Buffon, et partie du Cours complet d'histoire naturelle rédigé par C.S. Sonnini. 8. de l'imprimerie De F. Dufart, Paris, 439 pp. https://doi.org/10.5962/bhl.title.70894

De Jong JK, Brongersma LD (1927) Anatomische Notizen über *Varanus komodoensis* Ouwens. 1. Die Bewegungen im Schädel von *Varanus komodoensis*. Zoologischer Anzeiger 70: 65–69.

Dong L, Wang YQ, Zhao Q, Vasilyan D, Wang Y, Evans SE (2022) A new stem-varanid lizard (Reptilia, Squamata) from the early Eocene of China. Philosophical Transactions of the Royal Society B 377(1847): 1–19. https://doi.org/10.1098/rstb.2021.0041

English L (2017) Variation in crocodilian dorsal scute organization and geometry with a discussion of possible functional implications. Journal of Morphology 279(2): 154–162. https://doi.org/10.1002/jmor.20760

Frazzetta TH (1962) A functional consideration of cranial kinesis in lizards. Journal of Morphology 111(3): 287–319. https://doi.org/10.1002/jmor.1051110306

Frazzetta TH (1986) The origin of amphikinesis in lizards. In: Hecht MK, Wallace B, Prance GT (Eds) Evolutionary biology. Springer, Boston, MA, 419–461. https://doi.org/10.1007/978-1-4615-6983-1_8

Fry BG, Wroe S, Teeuwisse W, Van Osch MJP, Moreno K, Ingle J, Mchenry C, Ferrara T, Clausen P, Scheib H, Winter KL, Greisman L, Roelants K, Van Der Weerd L, Clemente CJ, Giannakis E, Hodgson WC, Luz S, Martelli P, Krishnasamy K, Kochva E, Kwok HF, Scanlon D, Karas J, Citron DM, Goldstein EJC, Mcnaughtan JE, Norman JA (2009) A central role for venom in predation by *Varanus komodoensis* (Komodo Dragon) and the extinct giant *Varanus* (*Megalania*) *priscus*. Proceedings of the National Academy of Sciences 106(22): 8969–8974. https://doi.org/10.1073/pnas.0810883106

Gauthier JA, Kearney M, Maisano JA, Rieppel O, Behlke ADB (2012) Assembling the squamate tree of life: Perspectives from the phenotype and the fossil record. Bulletin of the Peabody Museum of Natural History 53(1): 3–308. https://doi.org/10.3374/014.053.0101

Grimaldi D, Nguyen T, Ketcham R (2000) Ultra-high-resolution X-ray computed tomography (UHR CT) and the study of fossils in amber. In: Grimaldi D (Ed.) Studies on fossils in amber, with particular reference to the Cretaceous of New Jersey. Backhuys, Leiden, 77–91 pp.

Head JJ, Barrett PM, Rayfield EJ (2009) Neurocranial osteology and systematic relationships of *Varanus* (*Megalania*) *prisca* Owen, 1859 (Squamata: Varanidae). Zoological Journal of the Linnean Society 155(2): 445–457. https://doi.org/10.1111/j.10963642.2008.00448.x

Hildebrand M, Goslow GE (2004) Vergleichende und funktionelle Anatomie der Wirbeltiere. Springer Berlin Heidelberg, Berlin, Heidelberg, 713 pp. https://doi.org/10.1007/978-3-642-18951-7

Janeczek M, Goździewska-Harłajczuk K, Hrabska L, Klećkowska-Nawrot J, Kuropka P, Dobrzyński M, Melnyk O, Nikodem A (2023) Macroanatomical, histological and microtomographic study of the teeth of the Komodo Dragon (*Varanus komodoensis*)—adaptation to hunting. Biology 12(2): 247. https://doi.org/10.3390/biology12020247

Iordansky NN (2011) Cranial kinesis in lizards (Lacertilia): Origin, biomechanics, and evolution. Biology Bulletin 38(9): 868–877. https://doi.org/10.1134/S1062359011090032

Kirby A, Vickaryous M, Boyde A, Olivo A, Moazen M, Bertazzo S, Evans S (2020) A comparative histological study of the osteoderms in the lizards *Heloderma suspectum* (Squamata: Helodermatidae) and *Varanus komodoensis* (Squamata: Varanidae). Journal of Anatomy 236(6): 1035–1043. https://doi.org/10.1111/joa.13156

Klauber LM (1931) A new species of *Xantusia* from Arizona, with a synopsis of the genus. Transactions of the San Diego Society of Natural History 7(1): 1–16. https://doi.org/10.5962/bhl.part.6154

Klinkhamer AJ, Wilhite DR, White MA, Wroe S (2017) Digital dissection and threedimensional interactive models of limb musculature in the Australian Estuarine Crocodile (*Crocodylus porosus*). PLoS ONE 12(4): e0175079. https://doi.org/10.1371/journal.pone.0175079

Lee MSY (1996) Possible affinities between *Varanus giganteus* and *Megalania prisca*. Memoirs of the Queensland Museum 39(2): 232. https://www.biodiversitylibrary.org/page/40090225#page/94/mode/1up

Lee MSY (1997) The phylogeny of varanoid lizards and the affinities of snakes. Philosophical Transactions of the Royal Society B Biological Sciences 352(1349): 53–91. https://doi.org/10.1098/rstb.1997.0005

Linnaeus C (1758) Systema naturæ per regna tria naturæ, secundum classes, ordines, genera, species, cum characteribus, differentiis, synonymis, locis. Tomus I. Editio decima, reformata. Laurentii Salvii, Holmiæ, 824 pp. https://doi.org/10.5962/bhl.title.542

Lönnberg E (1928) Notes on *Varanus komodensis* Ouwens and its affinities. Arkiv för Zoologi 19A(27): 1–11.

Maisano JA, Bell CJ, Gauthier JA, Rowe T (2002) The osteoderms and palpebral in *Lanthanotus borneensis* (Squamata: Anguimorpha). Journal of Herpetology 36(4): 678–682. https://doi.org/10.2307/1565940

Maisano JA, Laduc TJ, Bell CJ, Barber D (2019) The cephalic osteoderms of *Varanus komodoensis* as revealed by high-resolution X-ray computed tomography. The Anatomical Record 302(10): 1675–1680. https://doi.org/10.1002/ar.24197

Marsh OC (1877) Notice of new dinosaurian reptiles from the Jurassic formations. The American Journal of Science and Arts 3(14): 514–516. https://doi.org/10.2475/ajs.s3-14.84.514

McCurry MR, Mahony M, Clausen PD, Quayle MR, Walmsley CW, Jessop TS, Wroe S, Richards H, Mchenry CR (2015) The Relationship between cranial structure, biomechanical performance and ecological diversity in Varanoid Lizards. PLoS ONE 10(6): e0130625. https://doi.org/10.1371/journal.pone.0130625

Mertens R (1942a) Die Familie der Warane (Varanidae). Erster Teil: Allgemeines. Abhandlungen der Senckenbergischen naturforschenden Gesellschaft 462: 1–116.

Mertens R (1942b) Die Familie der Warane (Varanidae). Zweiter Teil: Der Schädel Abhandlungen der Senckenbergischen naturforschenden Gesellschaft 465: 117–234.

Metzger KA (2002) Cranial kinesis in lepidosaurs: skulls in motion. In: Aerts P, D'Août K, Herrel A, Van Damme R (Eds) Topics in functional and ecological vertebrate morphology. Shaker Publishing, Maastricht, 15–46.

Moreno K, Wroe S, Clausen P, Mchenry C, D'Amore DC, Rayfield EJ, Cunningham E (2008) Cranial performance in the Komodo dragon (*Varanus komodoensis*) as revealed by high-resolution 3-D finite element analysis. Journal of Anatomy 212(6): 736–746. https://doi.org/10.1111/j.1469-7580.2008.00899.x

Ouwens PA (1912) On a large *Varanus* species from the island of Komodo. Bulletin du Jardin botanique de Buitenzorg 6: 1–3. https://www.biodiversitylibrary.org/page/3873564#page/323/mode/1up

Owen R (1859) Description of some remains of a gigantic land-lizard (*Megalania prisca*, Owen) from Australia. Philosophical Transactions of the Royal Society of London 149: 43–48. https://doi.org/10.1098/rspl.1879.0121

Pianka E, King D (2004) Varanoid lizards of the world. Indiana University Press, Bloomington, 641 pp. https://doi.org/10.2307/j.ctt-2005wjp

Purwandana D, Ariefiandy A, Imansyah MJ, Rudiharto H, Seno A, Ciofi C, Fordham DA, Jessop TS (2014) Demographic status of Komodo dragons populations in Komodo National Park. Biological Conservation 171:29–35. https://doi.org/10.1016/j.biocon.2014.01.017

Pyron R, Burbrink FT, Wiens JJ (2013) A phylogeny and revised classification of Squamata, including 4161 species of lizards and snakes. BMC Evolutionary Biology 13(1): 93. https://doi.org/10.1186/1471-2148-13-93

Rayfield EJ (2005) Aspects of comparative cranial mechanics in the theropod dinosaurs *Coelophysis*, *Allosaurus* and *Tyrannosaurus*. Zoological Journal of the Linnean Society 144(3): 309–316. https://doi.org/10.1111/j.1096-3642.2005.00176.x

Rayfield EJ, Norman DB, Horner CC, Horner JR, Smith PM, Thomason JJ, Upchurch P (2001) Cranial design and function in a large theropod dinosaur. Nature 409(6823): 1033–1037. https://doi.org/10.1038/35059070

Rieppel O (1978) The phylogeny and mechanics of the feeding apparatus in *Varanus* (Reptilia, Lacertilia). PhD Thesis, University of Basel, Basel, Germany.

Rieppel O (1979) A functional interpretation of the varanid dentition (Reptilia, Lacertilia Varanidae). Gegenbaurs morphologisches Jahrbuch 125(6): 797–817.

Rowe T, Brochu CA, Colbert M, Merck JW, Kishi K, Saglamer E, Warren S (1999) Introduction to alligator: Digital atlas of the skull. Journal of Vertebrate Paleontology 19: 1–8. https://doi.org/10.1080/02724634.1999.10011200

Shrivastava RK (1964) The structure and development of the chondrocranium of *Varanus*. II. The development of the orbito-temporal region. Journal of Morphology 115: 97–108. https://doi.org/10.1002/jmor.1051150107

Slaby O (1979) Morphogenesis of the nasal capsule, the nasal epithelial tube and the organ of Jacobson in Sauropsida. III. Morphogenesis of the nasal apparatus in a member of the family Varanidae. Folia Morphologica 27: 270–281.

Smith KK (1980) Mechanical significance of streptostyly in lizards. Nature 283: 778–779. https://doi.org/10.1038/283778a0

Snively E, Cotton JR, Ridgely R, Witmer LM (2013). Multibody dynamics model of head and neck function in *Allosaurus* (Dinosauria, Theropoda). Palaeontologia electronica 16(2): 1–29. https://doi.org/10.26879/338

Starck D (1979) Vergleichende Anatomie der Wirbeltiere auf evolutionsbiologischer Grundlage: Band 2: Das Skeletsystem: Allgemeines, Skeletsubstanzen, Skelet der Wirbeltiere einschließlich Lokomotionstypen. Springer Berlin Heidelberg, Berlin, Heidelberg, 784 pp. https://doi.org/10.1007/978-3-642-67159-3

Steindachner F (1878) Über zwei Eidechsen-Arten aus Süd-Amerika und Borneo. Denkschriften der Kaiserlichen Akademie der Wissenschaften. MathematischNaturwissenschaftliche Klasse 38: 93–96.

Uetz P, Freed P, Aguilar R, Reyes F, Kudera J, Hošek J [Eds] (2023) The Reptile Database http://www.reptile-database.org/ [accessed on 03. Nov. 2023]

Vickaryous MK, Meldrum G, Russell AP (2015) Armored geckos: A histological investigation of osteoderm development in *Tarentola* (Phyllodactylidae) and *Gekko* (Gekkonidae) with comments on their regeneration and inferred function. Journal of morphology 276(11): 1345–1357. https://doi.org/10.1002/jmor.20422

Westheide W, Rieger G (2015) Spezielle Zoologie. Teil 2: Wirbel- oder Schädeltiere. Springer Berlin Heidelberg, Berlin, Heidelberg, 711 pp.

Williams C, Kirby A, Marghoub A, Kéver L, Ostashevskaya-Gohstand S, Bertazzo S, Moazen M, Abzhanov A, Herrel A, Evans SE, Vickaryous M (2022) A review of the osteoderms of lizards (Reptilia: Squamata). Biological reviews of the Cambridge Philosophical Society 97(1): 1–19. https://doi.org/10.1111/brv.12788